Journal of Alloys and Compounds 923 (2022) 166185

Contents lists available at ScienceDirect

Journal of Alloys and Compounds

journal homepage: www.elsevier.com/locate/jalcom

Unveiling photoluminescent response of Ce-doped $CaCu_3Ti_4O_{12}$: An experimental-theoretical approach

H. Moreno[a,*], M. Damm[a], S.M. Freitas[b], M.V.S. Rezende[b], A.Z. Simões[a], G. Biasotto[c], V.R. Mastelaro[d], V.C. Teixeira[e], M.A. Ramirez[a]

[a] Sao Paulo State University – UNESP, Faculty of Engineering of Guaratingueta, Av. Dr. Ariberto Pereira da Cunha 333, Portal das Colinas, 12516-410 Guaratingueta, SP, Brazil
[b] Federal University of Sergipe (UFS) – Center for Exact Sciences and Technology (CCET), Department of Physics, Marechal Rondon s/n, Jardim Rosa Elze, 49100-000 Sao Cristovao, SE, Brazil
[c] São Paulo State University – UNESP, Chemistry Institute, Rua Prof. Francisco Degni, 55, Quitandinha, Araraquara, SP, Brazil
[d] São Carlos Institute of Physics, University of São Paulo, PO Box 369, 13560-970 São Carlos, SP, Brazil
[e] Brazilian Synchrotron Light Laboratory (LNLS), Brazilian Center for Research in Energy and Materials (CNPEM), 13083-970 Campinas, SP, Brazil

ARTICLE INFO

Article history:
Received 25 February 2022
Received in revised form 28 June 2022
Accepted 2 July 2022
Available online 5 July 2022

Keywords:
$CaCu_3Ti_4O_{12}$
Photoluminescence
Computing simulations
Optoelectronics
Ce-doped

ABSTRACT

$CaCu_3Ti_4O_{12}$: x% Ce (x = 0.00, 0.25, 0.50, 0.75, and 1.00) ceramic composites were prepared via solid-state reaction. Theoretical atomistic simulations were combined with experimental techniques to uncover Ce effects in the (micro)structure and photoluminescence of $CaCu_3Ti_4O_{12}$-based ceramics. Application of perovskites ceramics in optoelectronics have been limited by their specific, narrow emission range, which compromise operational efficiency, pushing for the development of novel perovskite-emissive materials. This study results confirm that Ce ions are incorporated at Ca sites within the $CaCu_3Ti_4O_{12}$ lattice, inducing point metal and oxygen vacancies in the optical bandgap region. Shallow-level defects ($V'_{Ca}/V^{\bullet\bullet}_{O}$) were associated with broadband violet-blue photoluminescent (PL) emissions. Better color rendering may be a direct consequence of crystalline field splitting/wider PL emission. Furthermore, results demonstrate that PL on $CaCu_3Ti_4O_{12}$: Ce system intensity can be modulated by structural defects, making it promising for applications in optoelectronics.

1. Introduction

Calcium copper titanate-based ($CaCu_3Ti_4O_{12}$) electronic ceramics have challenged scientists the [1] world over to improve charge and information storage and technology. $CaCu_3Ti_4O_{12}$ (CCTO) displays giant dielectric permittivity ($\varepsilon \sim 10^4$-10^5) over a wide frequency (10^{-2}–10^6 Hz) and temperature range (100–600 K) [2,3], enabling applications in dynamic random access memories (DRAM), multilayer ceramic capacitors (MLCCs), and microwave devices [4,5], varistors [6], sensors [7,8], optoelectronic [9,10], and magnetic devices [11,12], etc. Its distorted pseudo-perovskite structure with stoichiometric formula (AA')BO_3 formed by inclined [TiO_6] octahedra fosters the so-called Jahn-Teller effect [13].

Photoluminescence (PL) in CCTO-based ceramics is governed by its electronic structure, which is associated with structural symmetry, highly dependent on [TiO_6] cluster tilting and rotation due to O-Ti-O bond displacement, which can be significantly affected by charge density/mobility, light energy, as well as oxygen vacancy density [14,15]. Recent studies indicate that optical properties in CCTO-based ceramics arise from surface defects (e.g., Ti^{3+} and Cu^{2+}) and abundant oxygen vacancies, which not only shift the absorption response to the visible region but also reduces the electron–hole pair recombination. In previous work, this research group has revealed the possibility to produce tunable PL intensity and wavelength over the visible spectrum. Deep-level defects led to orange-red PL emissions, while shallow-level ones produced violet-blue emissions. On the other hand, vacancy-hole recombination was associated with blue-shift in samples with higher W content [16]. Thus, based on cerium covalency effect (Ce^{4+}/Ce^{3+}), the authors expect to observe metal/oxygen vacancy formation within the CCTO electronic structure. These intermediary energy levels (shallow and deep-level defects) associated with Ce-related $f \rightarrow d$ transitions may produce significant PL emission changes. On a phosphor, generally, a luminescence activator (e.g.: metallic ions, etc.) or intrinsic defect is incorporated into a microcrystalline host. Trivalent rare-earth ions

* Corresponding author.
E-mail address: hpiccolimoreno@gmail.com (H. Moreno).

https://doi.org/10.1016/j.jallcom.2022.166185
0925-8388/

(RE) stand out as luminescence activators as a result of their stable emissions associated with $f \rightarrow d/f \rightarrow f$ electronic transitions [17–19].

Released literature suggests a clear interdependence between CCTO-based ceramics structural point defects (e.g.: oxygen/metal vacancies) and their optoelectronic properties. Materials scientists have tried several methods to improve CCTO-based ceramic properties, such as CCTO matrix composite manufacturing [20–22], distinct synthesis methods [6,23–25], incorporation of alkaline-earth metals [26–28], etc. Finally, lanthanide family RE-doping (internal transition metals) [16,29,30] are known to work as luminescence centers within the host lattice, introducing extra energy levels within the electronic structure [15]. These energy levels act as traps, changing electronic excitation and de-citation dynamics. Dorenbos [31] reported the importance of RE defect *4f*-shell electron binding energy in wide band gap compounds relative to the binding energy valence electrons, determining the RE ion valence and RE ↔ host electrons/ holes transfer, which is a key mechanism in cerium activated scintillators [32,33].

Lanthanide-doping has been applied in the optoelectronics industry due to its capacity to create pure color emissions in chromaticity diagram borders (CIE - *Commission internationale de l'eclairage* 1931). Hence, these materials have been applied in photovoltaic devices, light-emitting diodes (LEDs), etc. Cerium stands out as the most abundant of lanthanides and is promptly reduced from Ce^{4+} to Ce^{3+}, leading to spontaneous oxygen vacancy formation within the CCTO structure [34]. Ce^{3+} ions are characterized by $4f^1 \leftrightarrow 5d^1$ optical transitions, allowed by spectroscopy selection rules, which can be recognized as broadband and may be displaced depending on crystalline field, whereas Ce^{4+} does not show optical activity due to its [Xe] electronic configuration.

In this study, a theoretical-experimental approach is used to investigate the influence of cerium in the PL response of CCTO: x% Ce (x = 0.00, 0.25, 0.50, 0.75, and 1.00) ceramic composites prepared via solid-state reaction, which to the best of the authors' knowledge has not been carried out so far. To do so, the energy solution for the insertion of Ce ions in the CCTO system was simulated. Shallow-level defects ($V'_{Ca}/V_{\delta}^{\bullet\bullet}$) were associated with broadband violet-blue photoluminescent (PL) emissions. Better color rendering may be a direct consequence of crystalline field splitting and wider PL emission. Furthermore, this study shows that PL on $CaCu_3Ti_4O_{12}$: Ce system intensity can be modulated by structural defects, making it promising for applications in optoelectronics.

2. Experimental procedure

2.1. Synthesis

$CaCu_3Ti_4O_{12}$ based-ceramic powders were prepared via solid-state reaction using $CaCO_3$ (99.9%; Sigma-Aldrich), TiO_2 (99.9%; Sigma-Aldrich) and CuO (99.9%; Sigma-Aldrich) as starting reagents. Cerium ions were added to the CCTO precursors mixture following the proportion of x wt% Ce (x = 0.00, 0.25, 0.50, 0.75, and 1.00) in the form of CeO_2 (99.9%; Sigma-Aldrich) powder. The oxide mixtures were ground using yttrium-stabilized zirconia spheres in an isopropyl alcohol suspension for 24 h, then they were taken to a fume hood for two hours and then dried in an oven for 12 h at 100 °C, deagglomerated in an agate mortar, and sifted in a 200-mesh sieve. All samples were calcined at 900 °C (~5 °C/min) for 12 h under air atmosphere, as determined by thermogravimetric analysis (TG-DTG) and Differential Thermal Analysis (DTA) (Seiko, model EXSTAR 6000) (Fig. S1-S2). After calcined, the powders were ground for 12 h, deagglomerated in an agate mortar, and sifted in a 200-mesh sieve to obtain a homogeneous powder.

2.2. Characterization

2.2.1. (Micro)structural characterization

X-ray powder diffraction (XRPD) was performed on a Bruker (model D8 Advance Eco) diffractometer, operating at 40 kV/25 mA (Cu - K_α radiation; λ_{Cu}≈1.5406 Å) over the $10 \le \theta \le 100°$ range (0.02° step size; 10 s/point collection time), and 0.6 mm receiving slit. *Rietveld* analysis was carried out using Topas Academic V5 [35] based on the Inorganic Crystal Structure Database (ICSD). Quantitative phase analysis, geometric, and *Rietveld* parameters (R_{Bragg}, $R_{wp,}$ R_{exp} and χ^2) were determined adjusting the background function to a Chebychev 4th order polynomial. Chemical surface analysis was performed on all samples using X-ray photoelectron spectroscopy (XPS) using a conventional XPS spectrometer (ScientaOmicron ESCA+) consisting of a high-performance hemispheric analyzer (EAC2000) and an Al K_α ($h\nu$=1486.6 eV) monochromatic excitation source. Analysis was performed under ultra-high vacuum (UHV) operating pressure ~ 10^{-9} Pa. XPS high-resolution spectra were recorded at constant pass energy (20 eV; 0.05 eV step size) using a charge neutralizer (CN10) to eliminate surface charging effects. XPS results were analyzed on CASA XPS.

Raman spectra for all samples were collected over the 150–1200 cm^{-1} at room temperature on a Horiba Jobin Yvon spectrophotometer (model LabRAM HR 800) equipped with an argon-ion laser (λ_{Ar} ≈ 532 nm; ~ 1.13 cm^{-1} step size). X-ray absorption (XAS) data were collected around the Ti (E_0 ≈ 4966 eV) and Cu (E_0 ≈ 8979 eV) K-edge at the X-ray Absorption beamlines (XAFS1/XAFS2) at the Brazilian Synchrotron Light Laboratory (LNLS/CNPEM, Campinas, Brazil). Experiments were performed on transmission mode using thin polymeric membranes. Ti/Cu-foils were used to calibrate the monochromator, while TiO_2 and Ti_2O_3, CuO and CuO_2 were used as reference materials for the measurements, at the Ti and Cu K-edge, respectively [36]. Three sequential scans were run for each sample in order to optimize the signal-to-noise ratio. The experimental data were analyzed using the ATHENA software [37].

Field-emission-gun coupled scanning electron microscopy (FEG-SEM) was performed on a Supra 35-VP microscope (Carl Zeiss) for evaluating particle size/morphology. Samples were dispersed on isopropanol, spread over a polyimide film, and dried under UV-light. Particle size distribution was determined using the software ImageJ [38].

2.2.2. Optical characterization

Photoluminescent response of all samples excited at 350 nm was measured at room temperature on a Fluorolog-3 FL3–122 (Horiba Jobin Yvon) over the 370–650 nm range. PL data were deconvoluted based on a Gaussian function. Finally, the associated points on the chromaticity diagram (CIE 1931) were obtained based on the PL spectrum for each sample (x = 0.00 – 1.00) using Origin® 2019.

2.3. Computational methods

Atomistic simulation based on the Coulombic and the short-range term of the Buckingham potential (Eq. 1) was used to perform static simulations, based on the Born model, to investigate the incorporation of Ce^{3+}, Ce^{4+}, and Ce^{3+}/Ce^{4+} ions within the CCTO structure.

$$U^{Buckingham} = A\exp\left(\frac{-r_{ij}}{\rho}\right) - \frac{C}{r_{ij}^6} \quad (1)$$

where $U^{Buckinhanm}$ is the Buckingham interatomic potential, A represents the repulsion between two ions i and j separated by a distance r, which is related to the size and "hardness" of the ions, ρ is

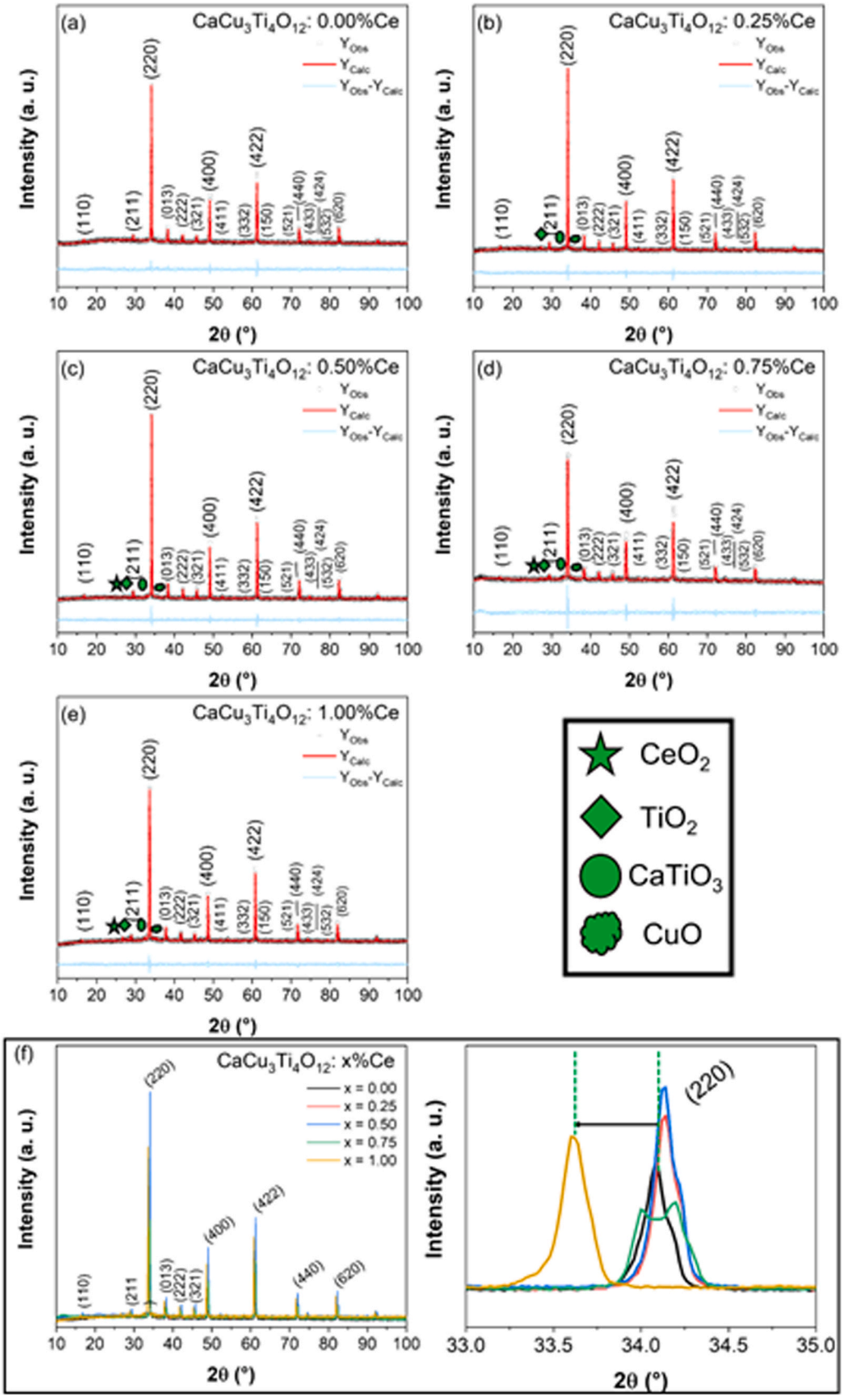

Fig. 1. XRPD patterns for all samples of the $CaCu_3Ti_4O_{12}$: Ce (x = 0.00–1.00) system (a) x = 0.00, (b) x = 0.25, (c) x = 0.50, (d) x = 0.75, and (e) x = 1.00 fitted using the *Rietveld* refinement method.

Table 1
Structural and Rietveld parameters for all samples of the CaCu3Ti4O12: Ce (x = 0.00 – 1.00) system.

Samples	CCTO			TiO_2		CTO		CuO		CeO_2		Rietveld parameters			
	V (Å^3)	phase (%)	R_{Bragg}	phase (%)	R_{Bragg}	phase (%)	R_{Bragg}	phase (%)	R_{Bragg}	phase (%)	R_{Bragg}	R_{exp}	R_{wp}	R_p	χ^2
x = 0.00	402.9	100.00	2.59	–	–	–	–	–	–	–	–	5.91	6.25	4.96	1.06
x = 0.25	403.4		2.34	2.18	1.44	2.61	1.72	2.44	1.28	–	–	5.20	5.51	4.35	1.06
x = 0.50	403.2	77.09	2.14	2.44	0.36	14.24	4.15	6.14	0.32	0.09	1.52	5.20	5.51	4.35	1.06
x = 0.75	403.6	85.78	1.69	2.02	0.51	8.26	1.19	3.46	0.63	0.46	1.21	5.52	6.53	5.09	1.18
x = 1.00	404.2	76.50	1.57	3.15	1.06	14.00	3.28	5.90	0.28	0.47	0.78	3.63	4.61	3.67	1.27

the minimum energy distance, and *C* is the term included to model the dispersion. The energy minimization procedure, which adjusts ionic positions in order to obtain the lowest energy structure, was adopted. The core-shell model is included to describe the ionic polarizability effect, in which the anions are divided into a massive core and a massless shell connected to a harmonic spring [39]. Defect calculations were performed using the Mott-Littleton methods, in which the crystal lattice is partitioned into a region in which relaxations close to the defect are treated explicitly, while the remainder of the lattice is treated using quasi-continuum methods [40]. For all calculations, the General Utility Lattice Program (GULP) code was used [41].

3. Results and discussion

3.1. (Micro)structural characterization

Fig. 1(a-e) shows XRPD patterns of the $CaCu_3Ti_4O_{12}$: Ce (x = 0.00–1.00) system. Sample x = 0.00 displayed pure CCTO standard crystal data (ICSD #259849) with cubic perovskite-type structure and space group *Im-3*. $CaCu_3Ti_4O_{12}$: Ce (x = 0.25–1.00) diffractograms revealed the formation of ceramic composites. Analogously to the sample with x = 0.00, diffraction peaks were well indexed by CCTO phase (ICSD #259849). On the other hand, these sample displayed peaks associated with TiO_2 (ICSD#33840, space group *P42/mnm*), CuO (ICSD#69094, space group *C12/c*), and $CaTiO_3$ (ICSD#74213, space group *Pbnm*). Furthermore, *Rietveld* analysis (Table 1) suggests incorporation of Ce ions at Ca sites within the CCTO structure, especially for x = 0.25. *Rietveld* analysis also suggests solid solution of Ce ions in the CCTO structure is limited to 0.50%, beyond which CeO_2 phase can be observed (ICSD #29046, with space group *Fm-3 m*) formation besides the structures mentioned (TiO_2, CuO and $CaTiO_3$). Ce ions are likely contributing to CeO_2 phase formation in the ceramic composite. Furthermore, its incorporation at Ca sites within the CTO structure becomes more relevant. Ca: Cu ratio adjustment leading to CCTO dissociation as a result of $Ce^{4+}\rightarrow Ce^{3+}$/$Ti^{4+}\rightarrow Ti^{3+}$ reactions may justify the presence of CTO, TiO_2, and CuO structures [42]. Table 1 shows all *Rietveld* and lattice parameters obtained for the $CaCu_3Ti_4O_{12}$: Ce system, and indicate a coherent, reliable refinement [16,27,43]. According to the *Rietveld* method, incorporation of Ce ions into Ca ions within the CCTO lattice leads to lattice expansion, which may result from the incorporation of Ce ions at Ca sites (for Coordination XII: R_{Ca2+}=1.34 Å, R_{Ce4+}=1.14 Å, R_{Ce3+}=1.34 Å) [44]. Fig. 1(f) illustrates this strong peak displacement towards lower 2θ values, indicating lattice expansion in the $CaCu_3Ti_4O_{12}$: Ce (x = 0.25–1.00) composites, especially for samples with x = 1.00. Additionally, XRPD analysis indicates that CCTO peak intensity decreases significantly in the $CaCu_3Ti_4O_{12}$: Ce (x = 0.25–1.00) composites compared to sample x = 0.00. Such a shift in peak position associated to peak intensity changes suggests the presence of defects in the CCTO crystal, which may be related to oxygen vacancies originated during the synthesis process. Even though Ce^{3+} and Ce^{4+} ions influence the host lattice in a different way, oxygen ion motion, promoted by the doping ions, caused crystallite expansion (See Table 1), which can be related to PL response.

Fig. 2(a-e) exhibits Ti *2p* high-resolution XPS spectra for all samples of the $CaCu_3Ti_4O_{12}$: Ce system (x = 0.00 – 1.00). Spectra unveils two main peaks, ~465 eV (Ti $2p_{3/2}$) and ~459 eV (Ti $2p_{1/2}$). These peaks were deconvoluted into spin-orbit doublet Ti state peaks (Ti^{4+} - TiO_2, and Ti^{3+} - Ti_2O_3, respectively) [45]. Based on fitting parameters, Ti^{4+}: Ti^{3+} ratio in the CCTO structure was estimated (Table 2). At ~459 eV, the main peak was ascribed to Ti^{4+} ions, and the secondary peak (~457 eV) to Ti^{3+} ions. Analogously to XRPD results, titanium tends to reduce ($Ti^{4+}+e^-\rightarrow Ti^{3+}$) increasing Ce content.

Fig. 3(a-e) shows Cu *2p* high-resolution XPS spectra for all the samples of the $CaCu_3Ti_4O_{12}$: Ce system (x = 0.00 – 1.00). The results reveal peaks associated with Cu $2p_{3/2}$ spin-orbit doublets (~933 eV) and its satellite peak (~941 eV). This feature indicates that the CCTO lattice contains Cu^{2+}/Cu^{+} ions simultaneously [45,46]. Cu $2p_{3/2}$ peak can be deconvoluted into two peaks related to Cu^{2+} at ~934.7 eV (CuO), and Cu^{+} at ~ 932.5 eV (Cu_2O) [47,48]. XPS data shows the simultaneous presence of Cu^{+}/Cu^{2+} ions within the CCTO structure, which is consistent with released literature [49]. Hence, its semiconductivity stems from electrons hopping between $Cu^{+}\leftrightarrow Cu^{2+}$ sites in the CCTO structure [50]. Table 2 shows Cu^{2+}:Cu^{+} ratio in the CCTO structure.

Finally, Fig. 3(f) exhibits Ce 3d high-resolution XPS spectra for sample with x = 1.00, which the authors believe to represent all other samples of the $CaCu_3Ti_4O_{12}$: Ce (x = 0.25–1.00) system. Sample x = 1.00 shows co-existence of Ce^{3+}/Ce^{4+} states associated with the presence of Ce $3d_{3/2}$ (~900 eV) and Ce $3d_{5/2}$ (~884 eV) peaks, related to two spin-orbit doublets originated from different configurations of the Ce^{4+} photoemission final state, and another two from Ce^{3+} lower oxidation state [51,52]. Compared to the other samples (x = 0.25–0.75), sample x = 1.00 presents a higher signal-to-noise ratio. Hence, even though the spectrum intensity is relatively low, and the noise level is high, it was possible to interpret the data and show the presence of Ce^{3+} and Ce^{4+} ions. Additionally, to corroborate these results, Energy Dispersive X-ray Spectroscopy (EDS) measurements were performed (Fig. S4), which confirm the presence of Ce ions in all samples.

Fig. 4(a) displays Raman spectra collected at room temperature for all samples of the $CaCu_3Ti_4O_{12}$: Ce (x = 0.00–1.00) system. All samples showed three out of the eight CCTO Raman active modes generally reported in the released literature. At 275 (F_g1), 440 (A_g1) and 552 (A_g2) cm^{-1}, M_1, M_3, and M_5, respectively, are all [TiO_6]-related vibrational modes [16,53,54]. M_5 can be associated with asymmetric coplanar O^{2-} ions vibration around Ti^{4+} ions in the [TiO_6] octahedra [54]. Modes M_3 (440 cm^{-1}), and M_6 (607 cm^{-1}) are generated by vertex joint octahedra interactions (folding, twisting, etc.). It is important to note that [TiO_6] clusters within the $CaTiO_3$ lattice may also contribute, proportionally, to the intensity of modes M_1,

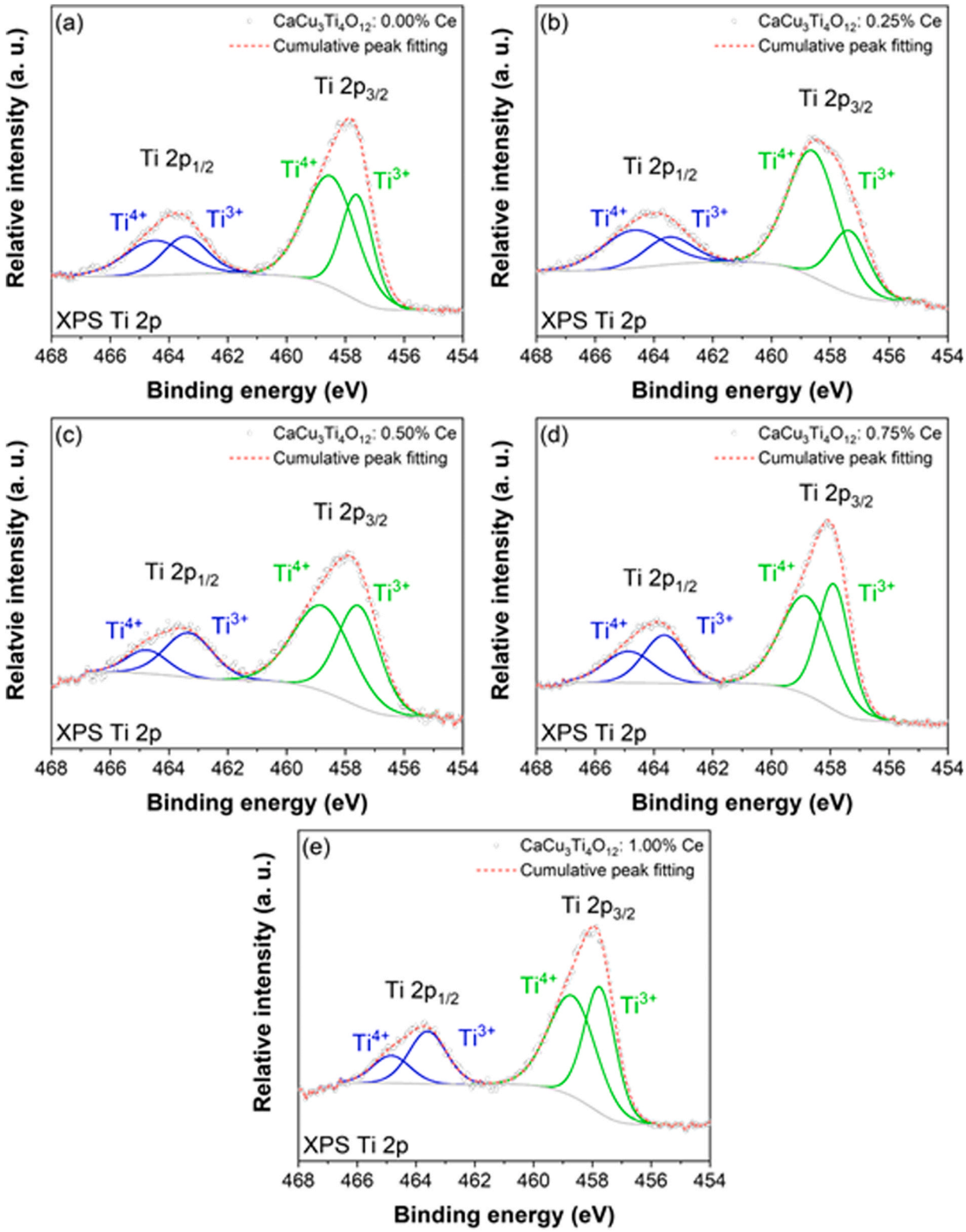

Fig. 2. (a–e) Ti 2p deconvoluted XPS spectra for all samples of the CaCu3Ti4O12: Ce (x = 0.00–1.00) system.

Table 2
XPS fitting parameters for all samples of the CaCu3Ti4O12: Ce (x = 0.00 – 1.00) system.

Samples	Ti^{4+}: Ti^{3+} ratio (%)	Cu^{2+}: Cu^{+} ratio (%)
x = 0.00	63.1: 36.9	82.3: 17.7
x = 0.25	72.6: 27.4	70.1: 29.9
x = 0.50	53.8: 46.2	91.6: 8.4
x = 0.75	55.7: 44.3	79.6: 20.4
x = 1.00	54.7: 45.3	86.5: 13.5

M_3, and M_5. M_1 and M_3 exhibit peak broadening for higher Ce contents (i.e., x = 0.50–1.00), which may result from $[TiO_6]$-related modes M_1 (~275 cm^{-1})/M_3 (~442 cm^{-1}) overlapping with $[CeO_8]$-related modes and M_2 and M_4 (~275 cm^{-1}), respectively, corroborating XRPD data [55,56]. This study's results also demonstrate slight M_3 red-shifts increasing Ce content, implying O–Ti–O stretching. Likewise, M_1 and M_5 Raman shifts indicate atomic motions in the $[TiO_6]$ clusters [57]. Finally, Table 3 compiles all vibrational modes observed for the composite samples of the $CaCu_3Ti_4O_{12}$: Ce (x = 0.00–1.00) system.

Fig. 4(b) depicts XANES spectra measured at the *Ti K-edge* for al samples of the $CaCu_3Ti_4O_{12}$: Ce (x = 0.00–1.00) system. Fig. 4(b) insert reveals pre-edge structures (peaks *A*, *B*, and *C*) associated with local symmetry/coordination of Ti ions within the CCTO lattice [58]. Peaks *A*, *B*, and *C* are all related to the octahedral nature of $[TiO_6]$ clusters, which constitute the CCTO structure, corroborating the Raman and XRPD data [59,60]. Two assumptions arise from pre-edge peak observations: occurrence of (1) Ti quadrupole *1 s* (occupied)→ *3d* (unoccupied) transitions; and (2) dipolar *1 s* (occupied)→*3d* (unoccupied) transition (relocation between neighboring sites in titanium atoms) [61]. Peak *A* (at ~4968 eV) results from two different mechanisms: potential *1 s*; and quadrupole transitions *1 s-3d* (absorption by octahedral t_{2g} band). Peak *B* (~4971 eV) suggests dipolar transitions to *p* states, and quadrupole *1 s→3d* transitions (absorption by the octahedral e_g band) [61–63]. Finally, peak *C* (~4974 eV) may be associated with electronic dipolar Ti *1 s→*t_{2g} transitions in adjacent $[TiO_6]$ octahedra [61–63]. Fig. 4(c) shows XANES spectra measured at the *Cu K-edge* of all samples of the $CaCu_3Ti_4O_{12}$: Ce (x = 0.00–1.00) system. An intense feature at ~8982 eV in the Cu_2O reference spectrum (hatched line labeled B) indicate dipole allowed *1 s→4p* transitions. This aspect works as a fingerprint for Cu^+ ion with d^0 configuration with no holes in the *3d* layer. Analogously for the CuO standard, one can observe a weak feature at ~8978 eV (hatched line labeled A), which is related to dipole forbidden *1 s→3d* transition, characteristic of Cu^{2+} ions in a $3d^9$ configuration [64]. For all samples, *Ti K-edge* energy position was between that of the standard samples (Ti_2O_3, Ti^{3+}, and TiO_2, Ti^{4+}, respectively). Likewise, *Cu K-edge* energy position was between Cu_2O (Cu^+) and CuO (Cu^{2+}), indicating the presence of Cu^+/Cu^{2+} and Ti^{3+}/Ti^{4+} oxidation states simultaneously across all samples. These results are consistent with XPS and XRPD data. Additionally, XRPD analysis suggests incorporation of Ce ions into Ca sites within the CCTO and CTO structures, which plays a key role in oxygen vacancy formation [64].

Fig. 5(a-f) displays FEG-SEM micrographs for all samples of the $CaCu_3Ti_4O_{12}$: Ce (x = 0.00–1.00) system and their respective particle size distribution (inserts). Apart from showing a mono-dispersed, submicrometric (~500 nm) particle size distribution, one can observe a decrease in mean particle size as with Ce content increases up to the solubility limit (x = 0.50), whereas for x = 0.75–1.00, mean particle size increases. These results may be associated with thermodynamic changes in the systems caused by CeO_2 phase formation. One can observe irregularly shaped, roundish particles with no significant changes to particles shape can be observed as a function of Ce content.

3.2. Defect calculations

The most probable site for the added Ce ions to occupy within the CCTO structure, and the associated charge-compensating defects (vacancies and interstitials), were estimated based on an energy-related approach. To do so, the formation energy associated with *Frenkel*, *Schottky*, and antisite disorders for Ce^{4+}/Ce^{3+} incorporation into different cationic sites within the CCTO structure (Ca^{2+}, Cu^{2+}, or Ti^{4+}) were calculated using static simulations, according to previously reported methodology [16,65,66]. Table 4 presents all intrinsic defect possibilities arranged in the form of *Kröger-Vink* equations, each with its associated solution energy. The highest solution energy intrinsic defects are those related to Ti at an interstitial position, Ti^{4+} *Frenkel*, and anti-*Schottky* defects, indicating these are not favorable defects to be formed considering Ce incorporation. On the other hand, Ca^{2+} pseudo-*Schottky* showed the lowest energy solution among all intrinsic defects, suggesting that $V_{Ca}^{'}$ associated with $V_O^{\bullet\bullet}$ has the highest probability for the CCTO structure. Comparatively, to account for Ce^{4+}/Ce^{3+} ion incorporation into the CCTO lattice, eighteen reactions were used to evaluate the most favorable incorporation scenario for Ce^{4+}→Ce^{3+} reducing Ce species. All defect reactions used to simulate Ce^{3+}, Ce^{4+}, and Ce^{4+}→Ce^{3+} incorporation within the CCTO lattice are displayed in Tables 5–7, according to the *Kröger-Vink* notation.

Fig. 6(a-c) show the solution energy associated with each possible defect reaction considered for incorporation of Ce^{3+}, Ce^{4+}, and Ce^{4+}→Ce^{3+}, respectively, within the CCTO lattice calculated following the same methodology reported in previous works [65–67]. Fig. 6(a) and Table 5 indicate that Ce^{3+} incorporation at Ca sites within the CCTO compensated by $V_{Ca}^{'}$ is the most favorable. Dopant ionic radius is key to determine incorporation site $R_{Ce3+} \approx R_{Ca2+}$, which suggests that Ce^{3+} ions may be incorporated at Ca^{2+} sites within the CCTO structure (CN: 12-R_{Ca2+}=1.34 Å, R_{Ce3+} =1.34 Å/R_{Ce4+}=1.14 Å; CN: 6–R_{Ti4+} = 0.60 Å, R_{Ce3+}=1.01 Å/R_{Ce4+}=0.87 Å, where CN represents the ion coordination number) [44]. Table 8 shows that Ce^{3+} incorporation at Ca/Cu sites causes less perturbation on first neighbors compared to Ce^{3+} incorporation at Ti^{4+} sites, which may even lead to lattice shrinkage.

Makcharoen et al. [68] showed a substantial mean grain size decrease with Ca^{2+} substitution for Ce^{3+} in CCTO ceramics. Similarly, Cheng et al. [49] suggested oxygen vacancy formation as charge-compensating defects for trivalent lanthanide doping at Ca^{2+} sites. Nonetheless, this study's results suggest Ca vacancies ($V_{Ca}^{'}$) as charge compensation for Ce ion incorporation. Fig. 6(b) and Table 6 also show Ce^{4+} incorporation at Cu/Ca sites compensated by $V_{Ca}^{'}$ have the lowest energy solution and, thus, are the most probable. This derives from $V_{Ca}^{'}$ high probability to spontaneously form within the CCTO lattice as intrinsic defects. Table 8 exhibits the local distortion around Ce^{4+} ions incorporated at each of the cationic sites in the CCTO structure considering its coordination. The CCTO lattice is not as affected by Ce^{4+} incorporation at Cu sites compared to Ce^{4+} substitution at Ca/Ti sites. Slighter change in interatomic distance for Ce^{4+}/Cu substitution compared to Ce^{4+}/Ca and Ce^{4+}/Ti may explain its lowest solution energy. Additionally, the largest difference in interatomic distance was obtained for Ce^{4+} ions incorporated at Ti

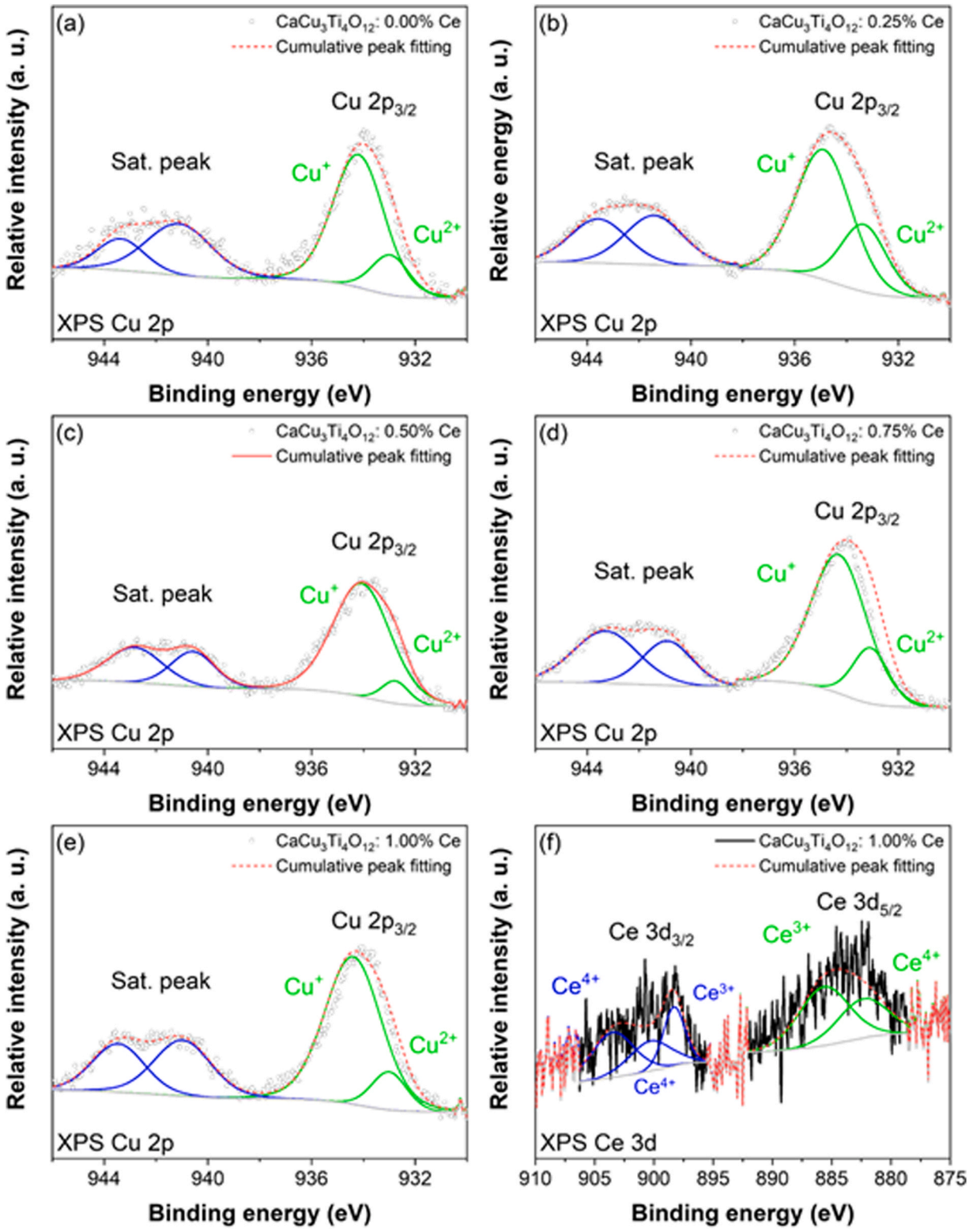

Fig. 3. (a–e) Cu 2p and (f) Ce 3d deconvoluted XPS spectra for all samples of the CaCu3Ti4O12: Ce (x = 0.25–1.00) system.

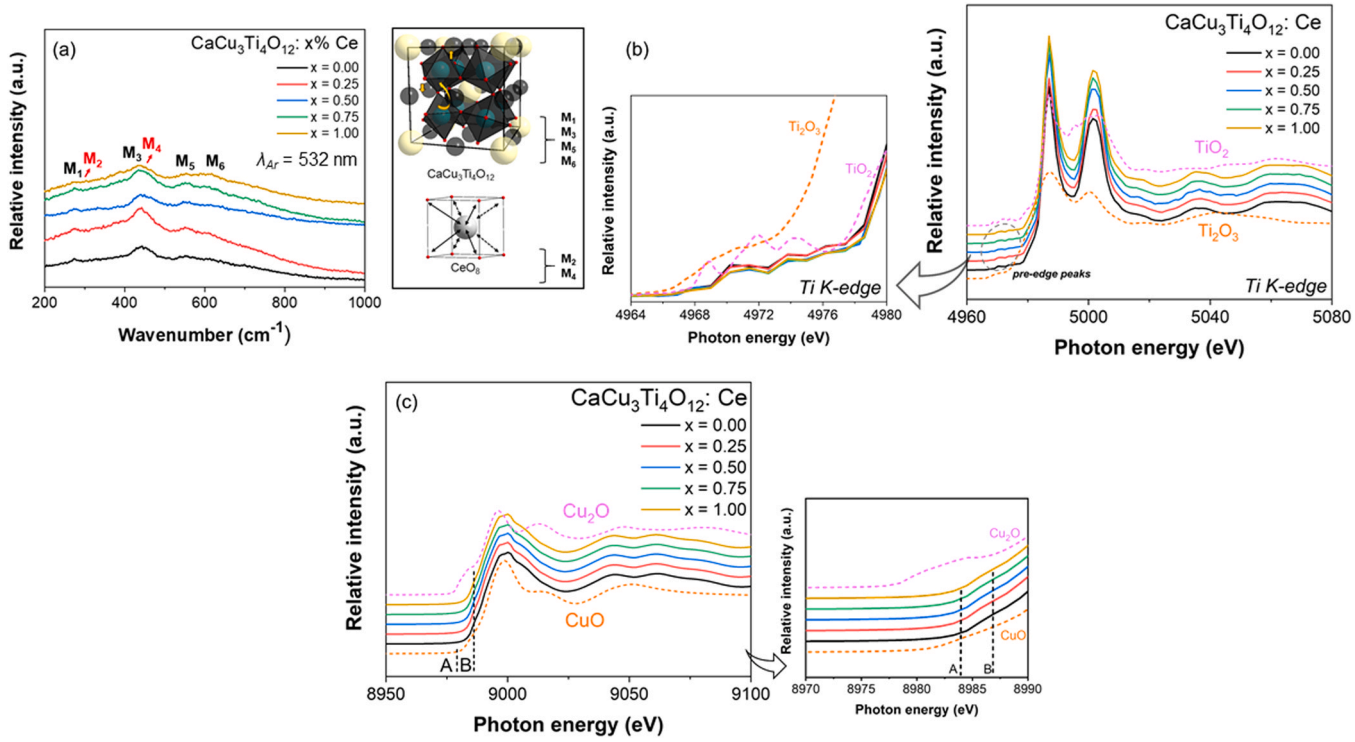

Fig. 4. (a) Raman spectra of the $CaCu_3Ti_4O_{12}$: Ce (x = 0.00 – 1.00) system; (b) *Ti K – edge* (inserts highlight pre-edge peaks); and (c) *Cu K – edge* XANES spectra obtained at room temperature for all samples of the $CaCu_3Ti_4O_{12}$: Ce (x = 0.00 – 1.00) system (the insert shows characteristic bands A and B).

Table 3
Raman shift and its associated mode/motion description for all samples of the CaCu3Ti4O12: Ce (x = 0.00 – 1.00) system.

$CaCu_3Ti_4O_{12}$	Mode	Motion description	Observed Raman shifts (cm^{-1})
	$F_g(1)$	TiO_6 rotation	~275
	$A_g(1)$	TiO_6 rotation	~442
	$F_g(3)$	O - Ti - O antisymmetric stretching	~551
CeO_2	–	transversely acoustic mode	~275
	$F_g(2)$	Ce – O symmetric vibration	~460
TiO_2	$A_g(1)$	O - Ti – O stretching	~610

sites (R_{Ti4+}=0.605 Å, R_{Cu2+}=0.570 Å, R_{Ca2+}=1.34 Å, R_{Ce4+}=0.870 Å) [44]. Preferred incorporation mechanism can be inferred comparing its corresponding energy solutions. According to Cheng et al. [51], on Ce^{4+}-doped CCTO, Cu^{+} formation is suppressed as confirmed by this paper's results.

The valence state of cerium can convert between Ce^{3+} in Ce_2O_3 and Ce^{4+} in CeO_2 due to its unique Ce^{3+}/Ce^{4+} redox couple [49]. For this reason, this study has investigated the possibility of Ce^{4+} reduction to Ce^{3+} at CCTO. Table 7 shows the schemes for Ce reduction, and the solution energy for each scheme is in Fig. 6(c). The most favorable scheme for Ce reduction is the incorporation at Ca site compensated by Ca vacancy (1.11 eV). The solution energy for Ce reduction (1.11 eV) is a little lower than that for the substitution of Ce^{4+} ion at Cu site compensated by an Ca vacancy (1.36 eV); this means that Ce^{4+} is more likely to reduce to Ce^{3+} than to remain Ce^{4+} in CCTO.

To estimate Ce solubility limit within the CCTO lattice, the concentration-dependent method reported by Rezende et al. [69] was used. Considering Ce incorporation within the CCTO lattice and the most probable substitution sites, adequate defect reactions and energy solutions equations for Ce^{3+} (Eqs. (2)–(4))/Ce^{4+} (Eqs. (5)–(7)) incorporation were developed, respectively. Simulated energy solution values for each of sample concentrations (x = 0.00–1.00) are summarized in Table 9.

$$0.5X\ Ce_2O_3 + (1 - 1.5X)CaO + 3CuO + 4TiO_2 \rightarrow (Ca_{1-3X/2}[V_{Ca}^{'}]_{X/2}Ce_X)Cu_3Ti_4O_{12} \quad (2)$$

$$E[(Ca_{(1-3X/2)}[V_{Ca}^{''}]_X Ce_X)Cu_3Ti_4O_{12}] = (1 - X)E[CaCu_3Ti_4O_{12}] + X/3E[2Ce_{Ca}^{\bullet} + V_{Ca}^{''}] \quad (3)$$

$$E_{Sol} = E[(Ca_{(1-3X/2)}[V_{Ca}^{''}]_X Ce_X)Cu_3Ti_4O_{12}] = (1 - X) - \{0.5XE_{latt}[Ce_2O_3] + (1 - 1.5X)E_{latt}[CaO] + 3E_{latt}[CuO] + 4E_{latt}[TiO_2]\} \quad (4)$$

$$X\ CeO_2 + (1 - X)CaO + (3 - X)CuO + 4TiO_2 \rightarrow Ca_X[V_{Ca}^{''}]_X (Cu_{(3-X/3)}Ce_{X/3})_3Ti_4O_{12} \quad (5)$$

$$E[Ca_X[V_{Ca}^{''}]_X(Cu_{(3-X/3)}Ce_{X/3})_3Ti_4O_{12}] = (1 - X)E[CaCu_3Ti_4O_{12}] + X/2E[Ce_{Ca}^{\bullet\bullet} + V_{Ca}^{''}] \quad (6)$$

$$E_{Sol} = E[Ca_{(1-X)}[V_{Ca}^{''}]_X(Cu_{(3-X/3)}Ce_{X/3})_3Ti_4O_{12} - \{XE_{latt}[CeO_4] + (1 - X)E_{latt}[CaO] + (3 - X)E_{latt}[CuO] + 4E_{latt}[TiO_2]\} \quad (7)$$

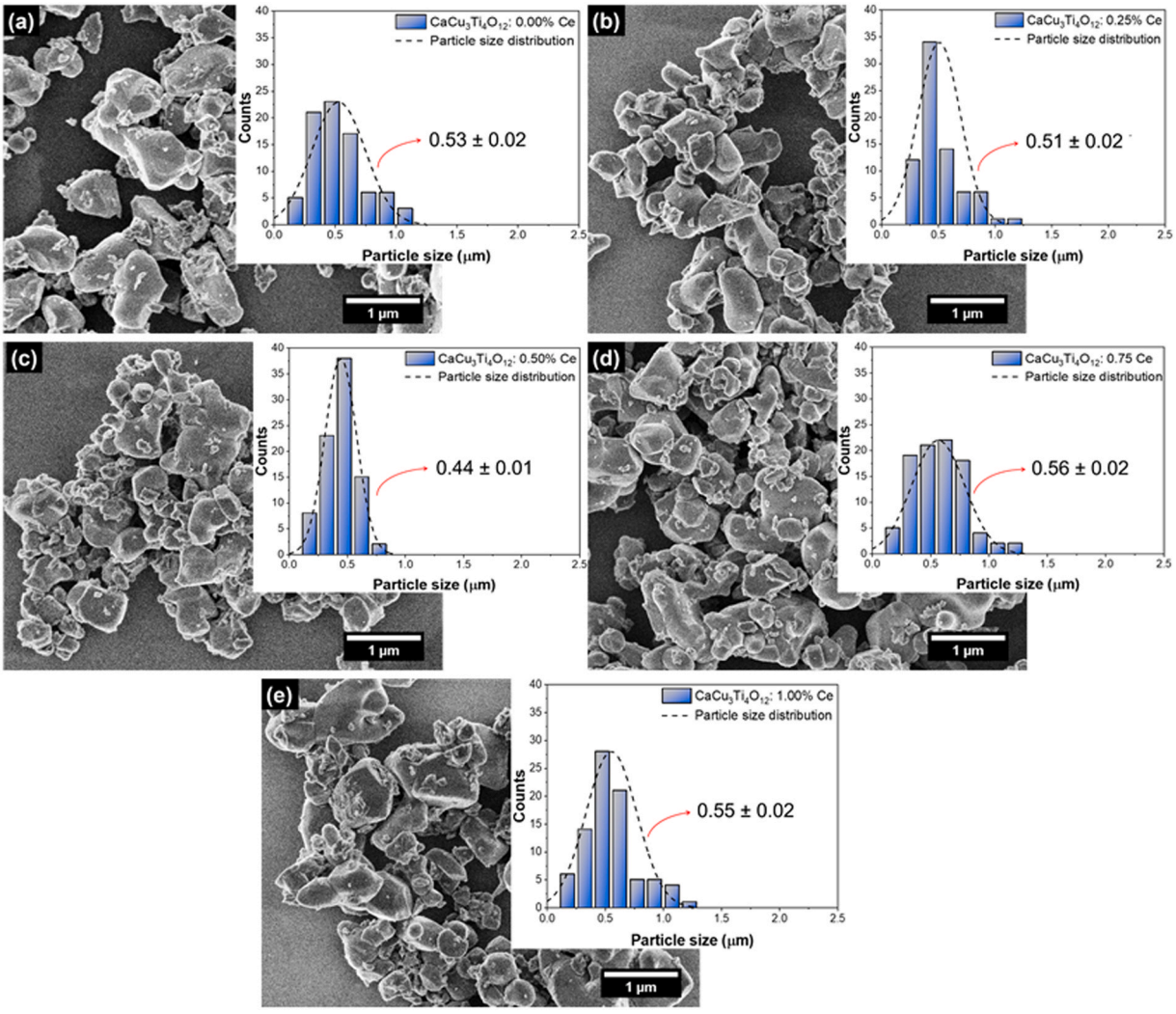

Fig. 5. FE-SEM micrograph images and particle size distribution for all samples of the $CaCu_3Ti_4O_{12}$: Ce (x = 0.00–1.00) system: (a) x = 0.00, (b) x = 0.25, (c) x = 0.50, (d) x = 0.75, (e), and x = 1.00. The inserts show particle size distribution.

Table 4
Intrinsic defect formation energies (eV/defect) in CaCu3Ti4O12.

Defect	Site	Reaction	Solution energy (eV)
Frenkel	Ca	$Ca_{Ca} \rightarrow V_{Ca}^{''} + Ca_i^{\bullet\bullet}$	7.00
	Cu	$Cu_{Cu} \rightarrow V_{Cu}^{''} + Cu_i^{\bullet\bullet}$	6.25
	Ti	$Ti_{Ti} \rightarrow V_{Ti}^{''''} + Ti_i^{\bullet\bullet\bullet\bullet}$	11.91
	O	$O_o \rightarrow V_o^{\bullet\bullet} + O_i^{''}$	4.82
Schottky	Total	$Ca_{Ca} + 3Cu_{Cu} + 4Ti_{Ti} + 12O_O \rightarrow V_{Ca}^{''} + 3V_{Cu}^{''} + 4V_{Ti}^{''''} + 12V_o^{\bullet\bullet} + CaCu_3Ti_4O_{12}$	3.07
Anti-Schottky	Total	$CaCu_3Ti_4O_{12} \rightarrow Ca_i^{\bullet\bullet} + 3Cu_i^{\bullet\bullet} + 4Ti_i^{\bullet\bullet\bullet\bullet} + 12O_i^{''}$	10.05
Pseudo Schottky	**Ca**	$\boldsymbol{Ca_{Ca} + O_o \rightarrow V_{Ca}^{''} + V_o^{\bullet\bullet} + CaO}$	**1.97**
	Cu	$Cu_{Cu} + O_o \rightarrow V_{Cu}^{''} + V_o^{\bullet\bullet} + CuO$	2.26
	Ti	$Ti_{Ti} + 2O_o \rightarrow V_{Ti}^{''''} + 2V_o^{\bullet\bullet} + TiO_2$	3.92
Antisítio	–	$Ca_{Ca} + Ti_{Ti} \rightarrow Ca_{Ti}^{''} + Ti_{Ca}^{\bullet\bullet}$	4.84
	–	$Cu_{Cu} + Ti_{Ti} \rightarrow Cu_{Ti}^{''} + Ti_{Cu}^{\bullet\bullet}$	2.33

Table 5
Kröger-Vink reactions for Ce3 + incorporation within the CaCu3Ti4O12 lattice and the associated energy solutions.

Site	Charge-compensator	Reaction	Solution Energy (eV)
Ca	1. **Ca vacancy**	$\boldsymbol{2Ce_2O_3 + 3Ca_{Ca} \rightarrow 2Ce^{\bullet}_{Ca} + V'''_{Ca} + 3CaO}$	**1.00**
	2. Cu vacancy	$Ce_2O_3 + 2Ca_{Ca} + Cu_{Cu} \rightarrow 2Ce^{\bullet}_{Ca} + V'_{Cu} + 2CaO + CuO$	1.19
	3. Ti vacancy	$2Ce_2O_3 + 4Ca_{Ca} + Ti_{Ti} \rightarrow 4Ce^{\bullet}_{Ca} + V''''_{Ti} + 4CaO + TiO_2$	1.97
	4. O interstitial	$Ce_2O_3 + 2Ca_{Ca} \rightarrow 2Ce^{\bullet}_{Ca} + O''_i + 2CaO$	2.90
	5. Antisite Ca'_{Ti}	$Ce_2O_3 + 2Ca_{Ca} + Ti_{Ti} \rightarrow 2Ce^{\bullet}_{Ca} + Ca'_{Ti} + CaO + TiO_2$	2.70
	6. Antisite Cu'_{Ti}	$Ce_2O_3 + CuO + 2Ca_{Ca} + Ti_{Ti} \rightarrow 2Ce^{\bullet}_{Ca} + Cu'_{Ti} + 2CaO + TiO_2$	1.28
Ti	7. Oxygen vacancies	$Ce_2O_3 + 2Ti_{Ti} + O_O \rightarrow 2Ce'_{Ti} + V^{\bullet\bullet}_{O} + 2TiO_2$	3.89
	8. Ca interstitial	$Ce_2O_3 + 2Ti_{Ti} + CaO \rightarrow 2Ce'_{Ti} + Ca^{\bullet\bullet}_i + 2TiO_2$	7.24
	9. Cu interstitial	$Ce_2O_3 + 2Ti_{Ti} + CuO \rightarrow 2Ce'_{Ti} + Cu^{\bullet\bullet}_i + 2TiO_2$	6.55
	10. Ti Interstitial	$2Ce_2O_3 + 4Ti_{Ti} \rightarrow 4Ce'_{Ti} + Ti^{\bullet\bullet\bullet\bullet}_i + 3TiO_2$	7.08
	11. Antisite ($Ti^{\bullet\bullet}_{Ca}$)	$Ce_2O_3 + 2Ti_{Ti} + Ca_{Ca} \rightarrow 2Ce'_{Ti} + Ti^{\bullet\bullet}_{Ca} + CaO + TiO_2$	5.00
	12. Antisite ($Ti^{\bullet\bullet}_{Cu}$)	$Ce_2O_3 + 2Ti_{Ti} + Cu_{Cu} \rightarrow 2Ce'_{Ti} + Ti^{\bullet\bullet}_{Cu} + CuO + TiO_2$	3.84
Cu	13. Ca vacancy	$Ce_2O_3 + 2Cu_{Cu} + Ca_{Ca} \rightarrow 2Ce^{\bullet}_{Cu} + V''_{Ca} + CaO + 2CuO$	1.12
	14. Cu vacancy	$Ce_2O_3 + 3Cu_{Cu} \rightarrow 2Ce^{\bullet}_{Cu} + V'_{Cu} + 3CuO$	1.31
	15. Ti vacancy	$2Ce_2O_3 + 4Cu_{Cu} + Ti_{Ti} \rightarrow 4Ce^{\bullet}_{Cu} + V''''_{Ti} + 4CuO + TiO_2$	2.11
	16. O interstitial	$Ce_2O_3 + 2Cu_{Cu} \rightarrow 2Ce^{\bullet}_{Cu} + O''_i + 2CuO$	3.02
	17. Antisite Ca'_{Ti}	$Ce_2O_3 + CaO + 2Cu_{Cu} + Ti_{Ti} \rightarrow 2Ce^{\bullet}_{Cu} + Ca'_{Ti} + 2CuO + TiO_2$	1.92
	18. Antisite Cu'_{Ti}	$Ce_2O_3 + 2Cu_{Cu} + Ti_{Ti} \rightarrow 2Ce^{\bullet}_{Cu} + Cu'_{Ti} + CuO + TiO_2$	1.40

Table 6
Kröger-Vink reactions for Ce4 + incorporation within the CaCu3Ti4O12 lattice and the associated energy solutions.

Site	Charge compensation	Reaction	Solution Energy (eV)
Ca	1. **Ca vacancy**	$\boldsymbol{CeO_2 + 2Ca_{Ca} \rightarrow Ce^{\bullet\bullet}_{Ca} + V''_{Ca} + 2CaO}$	**1.47**
	2. Cu vacancy	$CeO_2 + Cu_{Cu} + Ca_{Ca} \rightarrow Ce^{\bullet\bullet}_{Ca} + V'_{Cu} + CaO + CuO$	1.76
	3. Ti vacancy	$2CeO_2 + 2Ca_{Ca} + Ti_{Ti} \rightarrow 2Ce^{\bullet\bullet}_{Ca} + V''''_{Ti} + 2CaO + TiO_2$	3.25
	4. O interstitial	$CeO_2 + Ca_{Ca} \rightarrow Ce^{\bullet\bullet}_{Ca} + O''_i + CaO$	4.32
	5. Antisite Ca'_{Ti}	$CeO_2 + Ca_{Ca} + Ti_{Ti} \rightarrow Ce^{\bullet\bullet}_{Ca} + Ca'_{Ti} + TiO_2$	2.68
	6. Antisite Cu'_{Ti}	$CeO_2 + CuO + Ca_{Ca} + Ti_{Ti} \rightarrow Ce^{\bullet\bullet}_{Ca} + Cu'_{Ti} + TiO_2 + CaO$	1.89
Ti	7. Ce at Ti site	$CeO_2 + Ti_{Ti} \rightarrow Ce_{Ti} + TiO_2$	1.97
Cu	8. **Ca vacancy**	$\boldsymbol{CeO_2 + Cu_{Cu} + Ca_{Ca} \rightarrow Ce^{\bullet\bullet}_{Cu} + V''_{Ca} + CaO + CuO}$	**1.36**
	9. Cu vacancy	$CeO_2 + 2Cu_{Cu} \rightarrow Ce^{\bullet\bullet}_{Cu} + V'_{Cu} + 2CuO$	1.65
	10. Ti vacancy	$CeO_2 + 2Cu_{Cu} + Ti_{Ti} \rightarrow 2Ce^{\bullet\bullet}_{Cu} + V''''_{Ti} + 2CuO + TiO_2$	3.10
	11. O interstitial	$CeO_2 + Cu_{Cu} \rightarrow Ce^{\bullet\bullet}_{Cu} + O''_i + CuO$	4.21
	12. Antisite Ca'_{Ti}	$CeO_2 + CaO + Cu_{Cu} + Ti_{Ti} \rightarrow Ce^{\bullet\bullet}_{Cu} + Ca'_{Ti} + TiO_2 + CuO$	2.57
	13. Antisite Cu'_{Ti}	$CeO_2 + Cu_{Cu} + Ti_{Ti} \rightarrow Ce^{\bullet\bullet}_{Cu} + Cu'_{Ti} + TiO_2$	1.78

where E_{Sol} represents the energy solution, E_{latt} lattice formation energy, and X the element/ cluster molar proportion.

Ce solubility limit within the CCTO lattice is defined when the energy solution surpasses zero ($E_{Sol} \geq 0$). Considering x = 0.25% for both Ce^{3+} and Ce^{4+} addition, $E_{Sol} < 0$ (Table 9), hence the ions are readily soluble within the CCTO lattice. Increasing cerium content leads to an increase in E_{Sol} considering both Ce^{3+} and Ce^{4+} addition. For x = 0.50, $E_{Sol} > 0$, thus, solubility is not spontaneous for x ≥ 0.50. Therefore, our estimate shows that the maximum Ce^{3+} (Ce_2O_3) and Ce^{4+} (CeO_2) concentrations in which solid solution occurs (solubility limit) are 0.493 mol% and 0.490 mol%, respectively. *Rietveld* analysis showed CeO_2-phase formation only for samples with x ≥ 0.50–1.00, and little lattice distortion associated. Likewise, *Ti K-edge* XANES spectra revealed no significant changes, suggesting that Ce incorporation does not lead to severe distortions of [TiO_6] clusters within the CCTO lattice. Hence, atomistic simulations confirmed the experimentally measured structure of the $CaCu_3Ti_4O_{12}$: Ce (x = 0.00–1.00) system.

3.3. Optical characterization

Fig. 7(a-b) show the PL emission for all samples of the $CaCu_3Ti_4O_{12}$: Ce (x = 0.00–1.00) system excited at 350 and 400 nm, respectively, on a CIE 1931 chromaticity diagram. These results evidence broadening of the emission band (full-width half maximum, FWHM), which may result from PL quenching with Ce content increase. These results lead to improved color rendering, which is key in LED applications [70]. Furthermore, CIE diagram shows

Table 7
Kröger-Vink reactions for Ce4 + → Ce3 + incorporation within the CaCu3Ti4O12 lattice and the associated energy solutions.

Site	Charge compensation	Reaction	Solution Energy (eV)
Ca	1. **Ca vacancy**	$\boldsymbol{2CeO_2 + 3Ca_{Ca} \rightarrow 2Ce_{Ca}^{\bullet} + V_{Ca}^{''} + 3CaO + 0.5O_2}$	**1.11**
	2. Cu vacancy	$2CeO_2 + 2Ca_{Ca} + Cu_{Cu} \rightarrow 2Ce_{Ca}^{\bullet} + V_{Cu}^{''} + 2CaO + CuO + 0.5O_2$	1.31
	3. Ti vacancy	$4CeO_2 + 4Ca_{Ca} + Ti_{Ti} \rightarrow 4Ce_{Ca}^{\bullet} + V_{Ti}^{''''} + 4CaO + TiO_2 + 0.5O_2$	3.97
	4. O interstitial	$2CeO_2 + 2Ca_{Ca} \rightarrow 2Ce_{Ca}^{\bullet} + O_i^{''} + 2CaO + O_2$	6.65
	5. Antisite $Ca_{Ti}^{''}$	$2CeO_2 + 2Ca_{Ca} + Ti_{Ti} \rightarrow 2Ce_{Ca}^{\bullet} + Ca_{Ti}^{''} + CaO + TiO_2 + 0.5O_2$	2.88
	6. Antisite $Cu_{Ti}^{''}$	$2CeO_2 + CuO + 2Ca_{Ca} + Ti_{Ti} \rightarrow 2Ce_{Ca}^{\bullet} + Cu_{Ti}^{''} + 2CaO + TiO_2 + 0.5O_2$	1.39
Ti	7. Oxygen vacancies	$2CeO_2 + 2Ti_{Ti} + O_O \rightarrow 2Ce_{Ti}^{'} + V_O^{\bullet\bullet} + 2TiO_2 + 0.5O_2$	4.00
	8. Ca interstitial	$2CeO_2 + 2Ti_{Ti} + CaO \rightarrow 2Ce_{Ti}^{'} + Ca_i^{\bullet} + 2TiO_2 + 0.5O_2$	7.36
	9. Cu interstitial	$2CeO_2 + 2Ti_{Ti} + CuO \rightarrow 2Ce_{Ti}^{'} + Cu_i^{\bullet} + 2TiO_2 + 0.5O_2$	6.67
	10. Ti Interstitial	$4CeO_2 + 4Ti_{Ti} \rightarrow 4Ce_{Ti}^{'} + Ti_i^{\bullet\bullet\bullet\bullet} + 3TiO_2 + O_2$	11.26
	11. Antisite ($Ti_{Ca}^{\bullet\bullet}$)	$2CeO_2 + 2Ti_{Ti} + Ca_{Ca} \rightarrow 2Ce_{Ti}^{'} + Ti_{Ca}^{\bullet\bullet} + CaO + TiO_2 + 0.5O_2$	5.11
	12. Antisite ($Ti_{Cu}^{\bullet\bullet}$)	$2CeO_2 + 2Ti_{Ti} + Cu_{Cu} \rightarrow 2Ce_{Ti}^{'} + Ti_{Cu}^{\bullet\bullet} + CuO + TiO_2 + 0.5O_2$	3.96
Cu	13. **Ca vacancy**	$\boldsymbol{2CeO_2 + 2Cu_{Cu} + Ca_{Ca} \rightarrow 2Ce_{Cu}^{\bullet} + V_{Ca}^{''} + CaO + 2CuO + O_2}$	**1.23**
	14. Cu vacancy	$2CeO_2 + 3Cu_{Cu} \rightarrow 2Ce_{Cu}^{\bullet} + V_{Cu}^{''} + 3CuO + 0.5O_2$	1.42
	15. Ti vacancy	$4CeO_2 + 4Cu_{Cu} + Ti_{Ti} \rightarrow 4Ce_{Cu}^{\bullet} + V_{Ti}^{''''} + 4CuO + TiO_2 + O_2$	7.64
	16. O interstitial	$2CeO_2 + 2Cu_{Cu} \rightarrow 2Ce_{Cu}^{\bullet} + O_i^{''} + 2CuO + 0.5O_2$	3.13
	17. Antisite $Ca_{Ti}^{''}$	$2CeO_2 + CaO + 2Cu_{Cu} + Ti_{Ti} \rightarrow 2Ce_{Cu}^{\bullet} + Ca_{Ti}^{''} + 2CuO + TiO_2 + 0.5O_2$	2.04
	18. Antisite $Cu_{Ti}^{''}$	$2CeO_2 + 2Cu_{Cu} + Ti_{Ti} \rightarrow 2Ce_{Cu}^{\bullet} + Cu_{Ti}^{''} + CuO + TiO_2 + 0.5O_2$	1.51

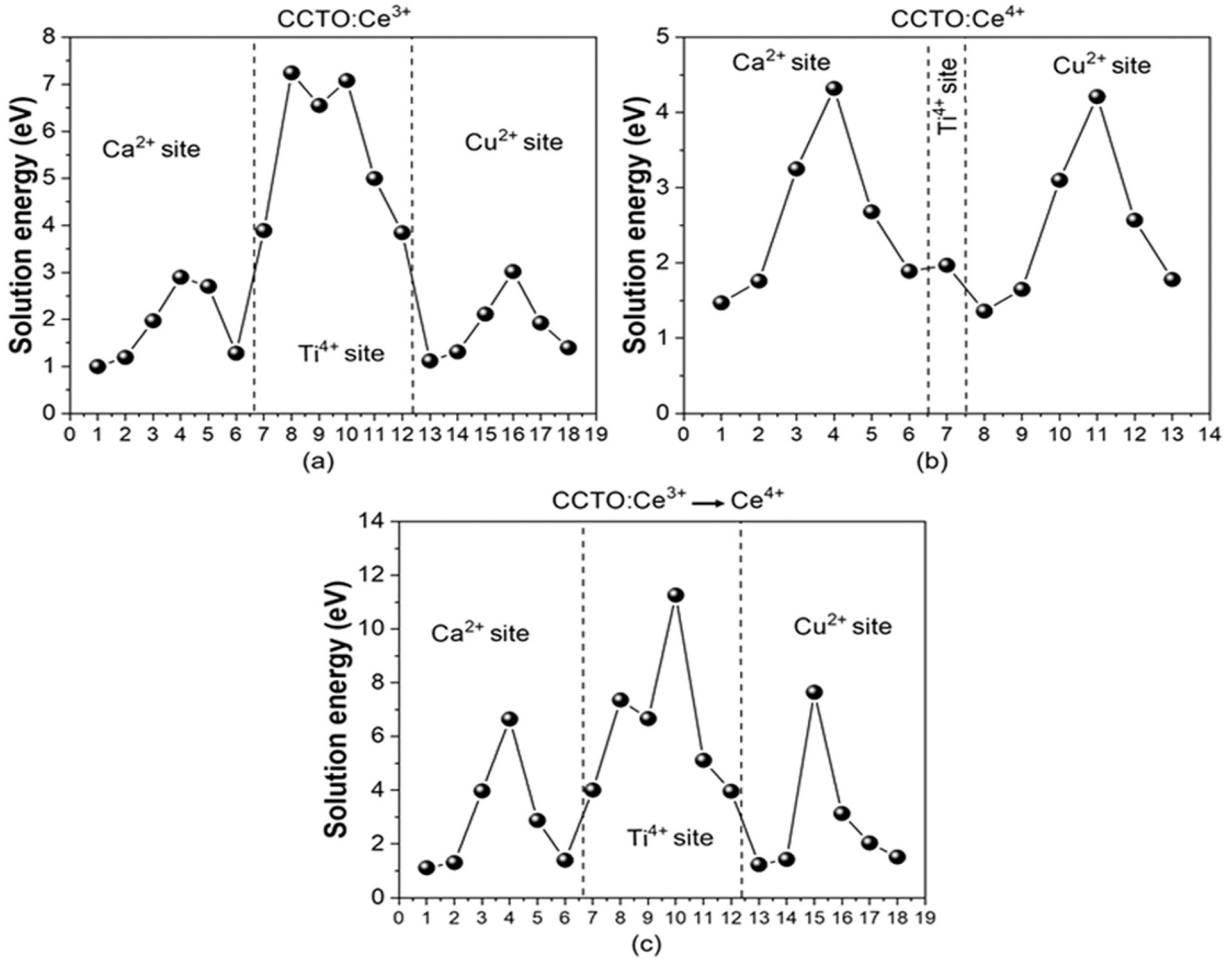

Fig. 6. Energy solution (a) Ce^{3+}; (b) Ce^{4+}; and (c) $Ce^{4+} \rightarrow Ce^{3+}$ incorporation at Ca, Cu, and Ti within the CCTO lattice.

Table 8
Interatomic distance changes considering Ce3 + and Ce4 + incorporation at Ca, Cu, and Ti sites within the CCTO lattice.

Ce^{3+} ions	$Ce^{\bullet}_{Ca}$	$Ce^{\bullet}_{Cu}$	Ce'_{Ti}
	Ce-O (x12)	Ce-O (x4)	Ce-O (x6)
	-0.02	0.24	0.38
Ce^{4+} ions	$Ce^{\bullet\bullet}_{Ca}$	$Ce^{\bullet\bullet}_{Cu}$	Ce_{Ti}
	Ce-O (x12)	Ce-O (x4)	Ce-O (x6)
	-0.15	0.05	0.21

Table 9
Solution energy for different Ce3 + and Ce4 + contents added to the CCTO lattice and solubility limit.

Valence state	0.25% CeO_2	0.50% CeO_2	0.75% CeO_2	1.00% CeO_2	Max. % CeO_2
Ce^{3+} ions	-3.12	-1.54	0.04	1.62	0.493
Ce^{4+} ions	-1.53	0.06	1.65	3.24	0.490

peripheral emissions when the samples are excited by a 350 nm source producing purer colors. On the other hand, the 400 nm excitation source produces PL emissions closer to the CIE diagram center for all samples (x = 0.00–1.00), thus indicating the contribution of different color centers in the gamut emission (white LED emissions).

Fig. 7(c-d) display PL emission spectra for all samples of the $CaCu_3Ti_4O_{12}$: Ce (x = 0.00–1.00) system excited at 350 and 400 nm, respectively. Samples excited at 350 nm exhibit intrinsic PL emissions on the violet-blue region (400–450 nm). Samples excited at 400 nm unveil typical intrinsic CCTO PL emissions on the green-orange region ($\lambda \approx$ 530–620 nm), as expected. These emissions can be associated with two main mechanisms: (1) CCTO gap transitions (CB→VB); and (2) defect-related transitions. Green emissions can be associated with gap transition (CB→VB) electron-hole pair recombination, which may be induced by light in CCTO. Intrinsic defects within CCTO electronic structure (i.e., V''_{Ca}, V''_{Cu}, $V^{\bullet\bullet}_{O}$, e', and $h^{\bullet}$) can be associated with violet-blue emissions (< 500 nm) (shallow-level defects near the VB and/or the CB) or red-infrared emissions (> 620 nm) (deep-level defects). Considering the presence of Ce^{3+} ions in $CaCu_3Ti_4O_{12}$: Ce, luminescence can be associated with exciton formation, while Ce^{4+} in $CaCu_3Ti_4O_{12}$: Ce, cannot interact positively with excitons due to its noble gas electronic configuration ([Xe]). Additionally, Ce^{4+} can re-absorb excitonic emissions through nonradiative mechanisms, negatively impacting on the light yield. That may be the reason why PL quenching can be observed for cerium doped samples (x > 0.00) [71]. The presence of Ce^{3+} ions with specific ground ([Xe]$4f^1$) and excited ([Xe]$5d^1$) state configurations may be identified by a symmetric, broad band, causing a blue shift on the PL emissions of samples with x > 0.00 [71]. Furthermore, cerium exhibits the so called nephelauxetic effect (covalency–Ce^{3+}/Ce^{4+}), which influences Ce^{3+} 5*d* energy levels resulting in greater crystalline field splitting [33,72]. Each of Ce^{3+} electronic states $5d^1$ (excited state) and $4f^1$ (ground state) is split by the crystal field into two (or more) components, namely $2D^{5/2}$ and $2D^{3/2}$ and $2F^{5/2}$ and $2F^{7/2}$, respectively, due to spin–orbit coupling [73]. Blue PL emissions (~460 nm) may be ascribed to CCTO bandgap excitation-recombination mechanisms.

Structural effects caused by Ce incorporation at Ca sites within the CCTO lattice can be observed in the PL spectra of samples x = 0.25–1.00. By increasing Ce content (x = 0.00–1.00), one can observe an increase in green emission, which may be associated with electron–hole/donor-acceptor charge transferring due to the formation of self-trapped charges within the optical bandgap region, but also to the presence of phase CuO/TiO_2 with intrinsic green PL emission, which contributes to producing different tones of blue PL emissions [16]. On the other hand, CTO phase also contributes to the red-orange PL emission due to its intrinsic characteristics [74]. Ce^{3+} $5d^1 \rightarrow 4f^1$ emission is generally centered at 520 nm; however, it is necessary to consider that Ce^{3+} emissions are highly dependent on host lattice. This study's results suggest that in the $CaCu_3Ti_4O_{12}$: Ce (x = 0.00–1.00) system Ce^{3+} $5d^1 \rightarrow 4f^1$ transitions occur around 460 nm, which explains broadening of the main PL emission peak and clarifies higher color rendering associated with Ce addition.

Several authors have observed strong blue emission in bulk CeO_2 (~422 nm), in which lower CeO_2 concentration led to peak displacement towards violet emissions (lower wavelengths). Authors associated these emissions to CeO_2 $4f \rightarrow$VB (valence band) transitions 9[73,75]. On bulk CeO_2, PL emission may be ascribed to photoreduction processes, leading to the simultaneous presence of Ce^{4+}/Ce^{3+}, and oxygen vacancy formation within the CeO_2 lattice. In the structure, Ce^{3+} ions tend to trap holes, while oxygen vacancies tend to trap electrons leading to broad associated emission [75]. These reports are consistent with this study's results, which show violet-blue emissions increase associated with CeO_2 phase formation, as corroborated by the XRPD analysis.

3.4. General discussion

Based on the PL response in Fig. 8(a), this study proposes a practical model to explain PL emission mechanisms for $CaCu_3Ti_4O_{12}$: Ce system considering the theoretical-experimental approach. One can observe emission quenching, which can be associated with electron-hole recombination. On the other hand, blue PL emission from Ce^{3+} increases as a result of CCTO bandgap excitation, leading to exciton creation and subsequent nonradiative recombination results in excitation from the ground $4f$ states to the excited $5d$ states on Ce^{3+} centers. CCTO-based ceramics PL emissions are driven by the presence of shallow and/or deep-level defects in the electronic structure of the material. PL results show direct electronic conduction (CB)→valence band (VB) emissions, and light generated electrons (e'), and holes ($h^{\bullet}$). Sample x = 0.00 exhibits larger red emission as a result of higher deep defect concentration compared to shallow defects. Fig. 8 exhibits a practical model used to explain PL emissions on $CaCu_3Ti_4O_{12}$: Ce system considering the theoretical simulations and experimental data (structural and optical measurements) presented in this paper, as well as considering RE and non-RE related trapping mechanisms. PL emission mechanisms of CCTO-based ceramics are strongly influenced by the presence of shallow/deep-level defects in the electronic structure as this research group has shown in previous studies [15,16]. In the case of $CaCu_3Ti_4O_{12}$: Ce

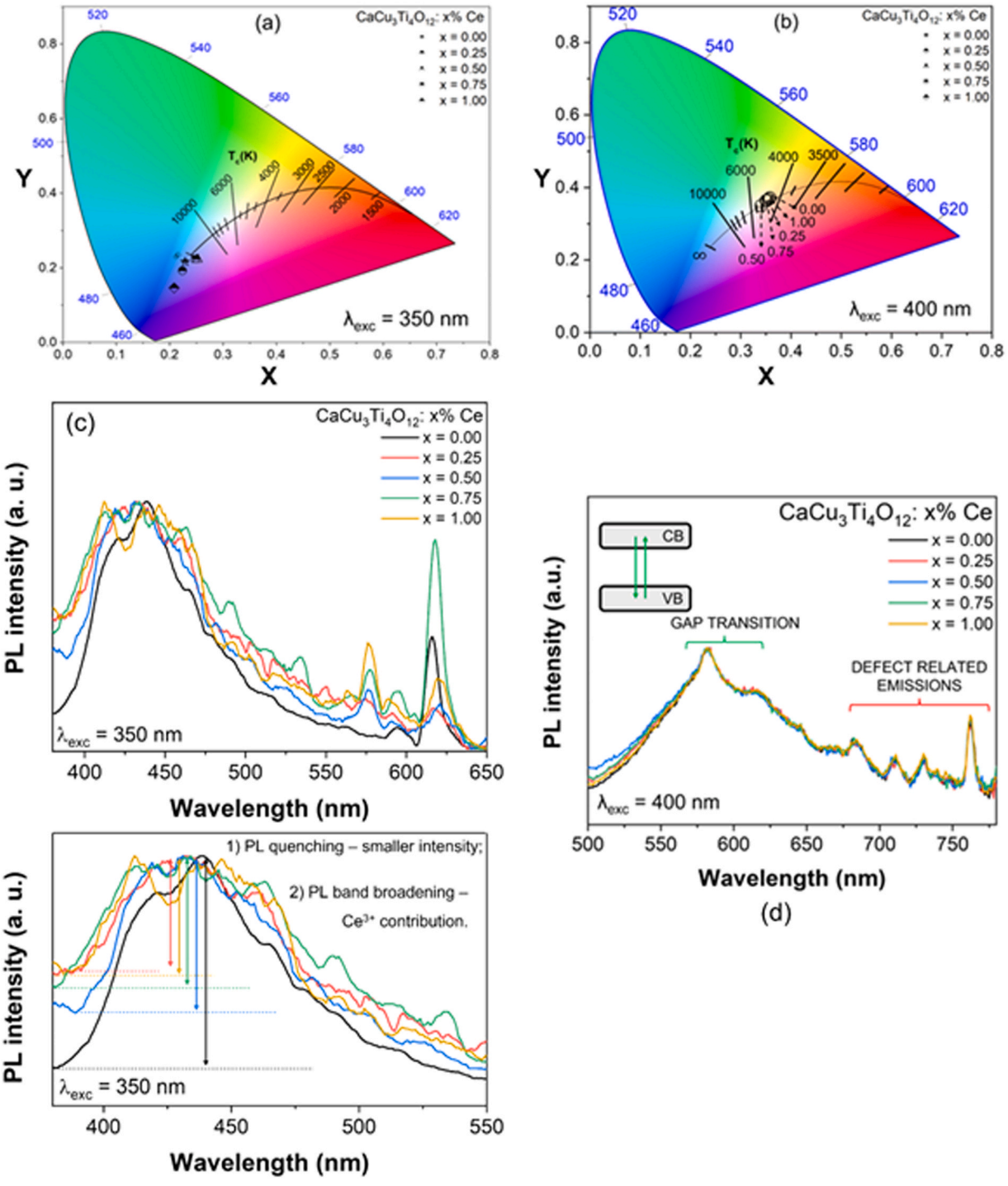

Fig. 7. Chromaticity diagram (CIE 1931) obtained for all samples of the $CaCu_3Ti_4O_{12}$: Ce (x = 0.00–1.00) system excited at (a) 350 and (b) 400 nm, and its respective PL emission spectra (c) 350 nm and (d) 400 nm excitation energy source.

system, apart from intrinsic defects, such as e', $h^{\bullet}$, $V_{Ca}^{''}$, and $V_{Cu}^{''}$, induced within the bandgap region both by Ce addition and light source excitation. Performed atomistic simulations revealed the presence of oxygen and metal vacancies ($V_{Ca}^{''}/V_{Cu}^{''}$), and local symmetry disruption with increasing Ce content, which was experimentally confirmed using XPS, Raman, and XAS. One can observe very specific Ce-related emissions: (1) Ce^{3+} has specific ground ([Xe] $4f^1$) and excited ([Xe]$5d^1$) state configurations, which are significantly dependent on chemical environment. In addition to crystalline field splitting, the nephelauxetic effect (covalency–Ce^{3+}/Ce^{4+}), which also influences $5d$ energy levels in Ce^{3+} ions resulting in a greater crystalline field splitting [76]. These results are confirmed by XPS analysis.

Fig. 8(b) considers the possible transitions in Ce^{3+} ($5d^1$ and $4f^1$), accounting for energy transfer mechanisms from CCTO excited by the light source. Intermediary energy levels in the CCTO: Ce optical bandgap induce electron-hole polaron formation. These traps within the optical bandgap energy region improve electron-hole ($e^- - h^{\bullet}$) recombination efficiency in the presence of metal/oxygen vacancies [77,78]. Considering Ce addition, Brito et al. [79] showed the importance of kinetics $4f^{n-1}$-$5d^1$ transitions lifetime of advanced persistent luminescence mechanisms for both RE^{2+} and RE^{3+} doping

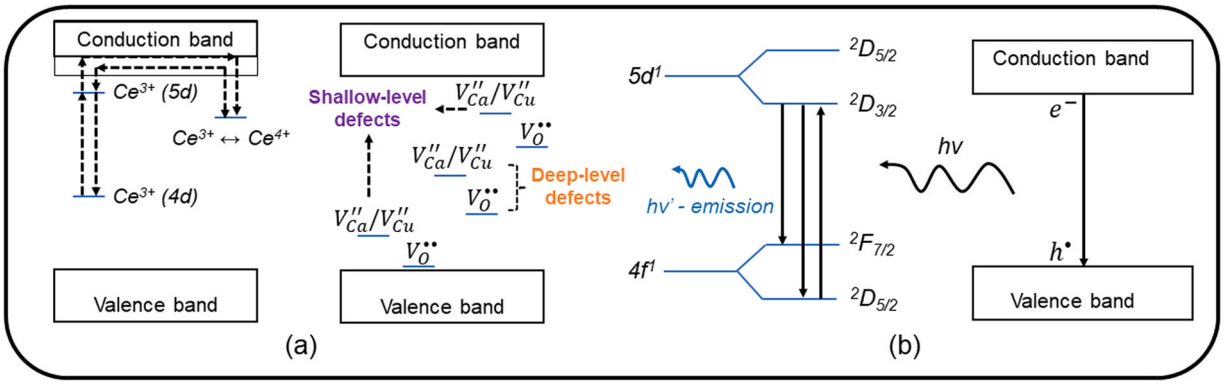

Fig. 8. (a) PL emission model for all samples of the $CaCu_3Ti_4O_{12}$: Ce (x = 0.00–1.00) system.

(~50 ns–1 μs). For CCTO doped with Ce^{3+}, short PL lifetime may be associated with competition between emission and electron hopping to the CCTO conduction band (CB)/trapping. Therefore, although energetically favorable, Ce^{3+}-doped compounds tend to present fluorescent response instead of persistent luminescence. The presence of Ce ions (RE) within the CCTO structure, make it necessary to consider an additional *kT* term due to its reduction mechanism (Ce^{4+}→Ce^{3+}). The term *kT* accounts for the energy necessary to overcome the thermal barrier at that defect level at a temperature *T* ($k \approx 1381 \times 10^{-23}$ J.K^{-1}, *Boltzmann* constant) to calculate PL efficiency, as proposed by Dorenbos *et. al.* [31].

4. Conclusion

This study uses an experimental-theoretical approach to provide strong evidence that Ce addition within the CCTO lattice is balanced by metal and oxygen vacancies (V_{Ca}'', V_{Cu}'', and $V_O^{\bullet\bullet}$, respectively). PL response of the $CaCu_3Ti_4O_{12}$: Ce system can be generally defined by CCTO gap transitions (CB→VB), and defect-related transitions (i.e., V_{Ca}'', V_{Cu}'', $V_O^{\bullet\bullet}$, e', and $h^{\bullet}$), which may be shallow-level defects – close to the valence or conduction bands – or deep-level defects – near the center of the bandgap region. Ce covalency (Ce^{4+}→Ce^{3+}) may be associated with PL active Ce^{3+} ions, which also increases oxygen vacancy density/mobility within the CCTO lattice. Additionally, intrinsic PL emission contributions of $CaTiO_3$ and TiO_2 phases must be considered. Broader, lower intensity violet-green PL emission related to Ce dependence on host lattice crystalline field suggests Ce^{3+} $5d^1 \rightarrow 4f^1$ transitions around 460 nm. Finally, CIE data reveals pure color (peripheral) emissions considering a 350 nm excitation source, and white color (centered) emissions for a 400 nm excitation source. Thus, this study's results provide clear theoretical-experimental evidence of the possibility to tune PL intensity and wavelength over the visible spectrum. Better color rendering may be a direct consequence of crystalline field splitting/wider PL emission, making $CaCu_3Ti_4O_{12}$: Ce ceramics a suitable choice to be applied in optoelectronics.

CRediT authorship contribution statement

H. Moreno: Preparation, Formal analysis, Methodology. **M. Damm:** Conceptualization, Methodology. **S. M. Freitas:** Formal analysis. **M.V.S. Rezende:** Formal analysis. **A. Z. Simões:** Formal analysis, Writing – review & editing. **G. Biasotto:** Methodology. **V. R. Mastelaro:** Formal analysis, Writing – review & editing. **V. C. Teixeira:** Formal analysis, Writing – review & editing. **M. A. Ramirez:** Conceptualization, Methodology, Supervision.

Data availability

Data will be made available on request.

Declaration of Competing Interest

The authors declare that they have no known competing financial interests or personal relationships that could have appeared to influence the work reported in this paper.

Acknowledgments

This work was financially supported by the Sao Paulo State Research Foundation (FAPESP) – process n. 2018/18236–4. The authors thank the Brazilian Synchrotron Light Laboratory (LNLS/CNPEM) for XAS measurements acquired at the XAFS1 and XAFS2 beamlines. FEG-SEM facilities were provided by LMA-IQ. We also thank the Brazilian National Nanotechnology Laboratory (LNNano/CNPEM) for the Horiba Fluoromax Plus (SisNANO) analyses, Lucas Carvalho Veloso Rodrigues from the Chemistry Institute (University of São Paulo), and João Batista Souza Junior (LNNano/CNPEM) for their valuable contributions.

Appendix A. Supporting information

Supplementary data associated with this article can be found in the online version at doi:10.1016/j.jallcom.2022.166185.

References

[1] Z. Tang, et al., **Significantly enhanced varistor properties of $CaCu_3Ti_4O_{12}$ based ceramics by designing superior grain boundary: Deepening and broadening interface states**, J. Mater. Sci. Technol. 108 (2022) 82–89.
[2] M.A. Subramanian, et al., **High Dielectric Constant in $ACu_3Ti_4O_{12}$ and $ACuTi_3FeO_{12}$ Phases**, J. Solid State Chem. 151 (2000) 323–325.
[3] X.J. Luo, et al., **Origin of the temperature stability of dielectric constant in $CaCu_3Ti_4O_{12}$**, Ceram. Int. 45 (2019) 12994–13003.
[4] S. Kaur, et al., Dielectric and energy storage behavior of CaCu 3 Ti 4 O 12 nanoparticles for capacitor application, Ceram. Int. 45 (2019) 7743–7747.
[5] C. Sripakdee, et al., **Very high-performance dielectric and non-ohmic properties of novel X8R type $Ca_{1-1.5x}Ho_xCu_3Ti_4O_{12}/TiO_2$ ceramics**, J. Alloy Compd. 779 (2019) 521–530.
[6] J. Wang, et al., **Excellent capacitor-varistor properties in lead-free $CaCu_3Ti_4O_{12}$-$SrTiO_3$ system with a wrinkle structure via interface engineering**, ACS Appl. Mater. Interfaces 12 (2020) 48781–48793.
[7] A. Natkaeo, et al., **Highly selective sub–10 ppm H_2S gas sensors based on Ag-doped $CaCu_3Ti_4O_{12}$ films**, Sens. Actuators B: Chem. 260 (2018) 571–580.
[8] A. Chattopadhyay, J. Nayak, **Improvement of humidity sensing performance and dielectric response through pH variation in $CaCu_3Ti_4O_{12}$ ceramics**, Sens. Actuators A: Phys. (341 () (2022) Article 113603.
[9] N.U. Saqib, et al., **An emerging photocatalyst for wastewater remediation: a mini-review on $CaCu_3Ti_4O_{12}$ photocatalysis**, Environ. Sci. Pollut. Res. 29 (2022) 40403–40414.

[10] M. Wang, et al., **Sonocatalysis and sono-photocatalysis in $CaCu_3Ti_4O_{12}$ ceramics**, Ceram. Int. 48 (2022) 11338–11345.
[11] F.M. Praxedes, et al., **Interface matters: Design of an efficient $CaCu_3Ti_4O_{12}$-rGO photocatalyst**, Powder Technol. (404 () (2022) Article 117478.
[12] N.A. Zhuk, et al., **Thermal behavior, magnetic properties, ESR, XPS, Mössbauer and NEXAFS study of Fe-doped $CaCu_3Ti_4O_{12}$ ceramics**, J. Alloy Compd. (855) (2021) Article 157400.
[13] N.A. Zhuk, et al., **Magnetic susceptibility, XPS and NEXAFS spectroscopy of Ni-doped $CaCu_3Ti_4O_{12}$ ceramics**, Mater. Chem. Phys. (252) (2020) Article 123310.
[14] P.Y. Raval, et al., **Effect of thermal history on structural, microstructural properties and J – E characteristics of $CaCu_3Ti_4O_{12}$ polycrystalline ceramic**, Mater. Chem. Phys. 212 (2018) 343–350.
[15] S. Orrego, et al., **Photoluminescence behavior on Sr^{2+} modified $CaCu_3Ti_4O_{12}$ based ceramics**, Ceram. Int. 44 (2018) 10781–10789.
[16] H. Moreno, et al., **Tunable photoluminescence of $CaCu_3Ti_4O_{12}$ based ceramics modified with tungsten**, J. Alloy Compd. (850) (2021) Article 156652.
[17] D. Poelman, D. van der Heggen, J. Du, E. Cosaert, P.F. Smet, Persistent phosphors for the future: Fit for the right application, J. Appl. Phys. (128) (2020) Article 240903.
[18] Z. Xia, A. Meijerink, **Ce^{3+}-Doped garnet phosphors: Composition modification, luminescence properties and applications**, Chem. Soc. Rev. 46 (2017) 275–299.
[19] J. Meyer, F. Tappe, Photoluminescent materials for solid-state lighting: State of the art and future challenges, Adv. Opt. Mater. 3 (2015) 424–430.
[20] L. Variar, et al., **High dielectric constant and low-loss, carbon black/$CaCu_3Ti_4O_{12}$/epoxy composites for embedded capacitor applications**, Mater. Res. Bull. (152) (2022) Article 111835.
[21] H. Wu, et al., **Precise regulation of weakly negative permittivity in $CaCu_3Ti_4O_{12}$ metacomposites by synergistic effects of carbon nanotubes and graphene**, Adv. Compos. Hybrid Mater 5 (2022) 419–430.
[22] G. Miao, et al., **Analysis of complex impedance and electrical conductivity of $YCr_{0.5}Mn_{0.5}O_3$–$CaCu_3Ti_4O_{12}$ negative temperature coefficient ceramics**, Ceram. Int. (2022).
[23] E.C. Grzebielucka, et al., **Improvement in varistor properties of $CaCu_3Ti_4O_{12}$ ceramics by chromium addition**, J. Mater. Sci. Technol. 41 (2020) 12–20.
[24] J. Boonlakhorn, et al., **Giant dielectric properties of Mg doped $CaCu_3Ti_4O_{12}$ fabricated using a chemical combustion method: Theoretical and experimental approaches**, Mater. Res. Bull. (150) (2022) Article 111749.
[25] B. Yadav, et al., Impact of defect migration on electrical and dielectric properties in molten salt synthesized $CaCu_3Ti_4O_{12}$ and customizing the properties by compositional engineering with Mg doping, Mater. Chem. Phys. (281) (2022) Article 125893.
[26] R.M. Ramadan, et al., **New approach for synthesis of nano-sized $CaCu_3Ti_4O_{12}$ powder by economic and innovative method**, J. Mater. Sci.: Mater. Electron. 31 (2020) 9065–9075.
[27] A.A. Felix, et al., **Enhanced electrical behavior in $Ca_{1-x}Sr_xCu_3Ti_4O_{12}$ ceramics**, Ceram. Int. 45 (2019) 14305–14311.
[28] J.A. Cortés, et al., **Dielectric and non-ohmic properties of $Ca_2Cu_2Ti_{4-x}Sn_xO_{12}$ (0.0 ≤ x ≤4.0) multiphasic ceramic composites**, J. Alloy Compd. 735 (2018) 140–149.
[29] K.K. Jani, et al., **Ca^{2+}-substitution effect on the electronic structure of $CaCu_3Ti_4O_{12}$ studied by electron spectroscopy for chemical analysis**, Ceram. Int. 47 (2021) 5542–5548.
[30] J. Boonlakhorn, P. Srepusharawoot, P. Thongbai, **Distinct roles between complex defect clusters and insulating grain boundary on dielectric loss behaviors of (In3+/Ta5+) co-doped $CaCu_3Ti_4O_{12}$ ceramics**, Results Phys. (16) (2020) Article 102886.
[31] N.A. Zhuk, et al., **Electrical properties of Ni-doped $CaCu_3Ti_4O_{12}$ ceramics**, Solid State Ion. (364) (2021) Article 115633.
[32] P. Dorenbos, A review on how lanthanide impurity levels change with chemistry and structure of inorganic compounds, ECS J. Solid State Sci. Technol. 2 (2013) R3001–R3011.
[33] K. Igashira, et al., Photoluminescence, scintillation and thermoluminescence properties of Ce-doped SrLaAl3O7 crystals synthesized by the optical floating zone method, Opt. Mater. (112) (2021) Article 110782.
[34] H. Fukushima, et al., Photoluminescence and scintillation properties of Ce-doped SrLu2O4 single crystals, Solid State Sci. (110) (2020) Article 106471.
[35] Y. Hanajiri, et al., EXAFS analyses of CaTiO3 doped with Ce, Nd and U, Solid State Ion.-. 108 (1998) 343–348.
[36] A.A. Coelho, TOPAS and TOPAS-Academic: An optimization program integrating computer algebra and crystallographic objects written in C++, J. Appl. Crystallogr. 51 (2018) 210–218.
[37] H.C.N. Tolentino, et al., **A 2.3 to 25 KeV XAS beamline at LNLS**, J. Synchrotron, Rad 8 (2001) 1040–1046.
[38] B. Ravel, M.Newville ATHENA, ARTEMIS, HEPHAESTUS: data analysis for X-ray absorption spectroscopy using IFEFFIT, J. Synchrotron Rad. 12 (2005) 537–541.
[39] A. Bertran, et al., Particle size determination from magnetization curves in reduced graphene oxide decorated with monodispersed superparamagnetic iron oxide nanoparticles, J. Colloid Interface Sci. 566 (2020) 107–119.
[40] B.G. Dick, A.W. Overhauser, Theory of the Dielectric Constants of Alkali Halide Crystals, Phys. Rev. 112 (1958) 90–103.
[41] B. Hadjarab, A. Bouguelia, M. Trari, **Synthesis, physical and photo electrochemical characterization of La-doped $SrSnO_3$**, J. Phys. Chem. Solid 68 (2007) 1491–1499.
[42] J.D. Gale, GULP: A computer program for the symmetry-adapted simulation of solids, Faraday 93 (1997) 629–637.
[43] M.A. Ramirez, et al., **Non-Ohmic and dielectric properties of a $Ca_2Cu_2Ti_4O_{12}$ polycrystalline system**, Appl. Phys. Lett. 89 (2006) 87–90.
[44] A. Dinnebier, J.S.O.E. De Gruyter, Rietveld Refinement Pract. Powder Diffr. Pattern Anal. Using TOPAS 52 (2019) 1238–1239.
[45] R.D. Shannon, Revised effective ionic radii and systematic studies of interatomic distances in halides and chalcogenides, Acta Crystallogr A32 (1976) 751–767.
[46] U.M. Meshiya, et al., **Electronic structure, orbital symmetry transformation, charge transfer, and valence state studies on Fe^{3+}-substituted $CaCu_3Ti_4O_{12}$ quadruple perovskites using X-ray photoelectron spectroscopy**, Ceram. Int. 46 (2020) 2147–2154.
[47] J. Jumpatam, **Giant dielectric behavior of monovalent cation / anion (Li^+, F^-)**, J. Am. Ceram. Soc. 103 (2020) 1871–1880.
[48] J. Jumpatam, N. Chanlek, P. Thongbai, **Giant dielectric response, electrical properties and nonlinear current-voltage characteristic of Al_2O_3-$CaCu_3Ti_4O_{12}$ nanocomposites**, Appl. Surf. Sci. 476 (2019) 623–631.
[49] C.R. Foschini, et al., Evidence of ferroelectric behaviour in CaCu 3 Ti 4 O 12 thin films deposited by RF-sputtering, Proc. Appl. Ceram. 13 (2019) 219–228.
[50] B. Cheng, Y.H. Lin, W. Deng, J. Cai, J. Lan, C.W. Nan, X. Xiao, J. He, **Dielectric and nonlinear electrical behaviors of Ce-doped $CaCu_3Ti_4O_{12}$ ceramics**, J. Electroceram. 29 (2012) 250–253.
[51] K.K. Jani, et al., **Ca^{2+}-substitution effect on the electronic structure of $CaCu_3Ti_4O_{12}$ studied by electron spectroscopy for chemical analysis**, Ceram. Int. 47 (2021) 5542–5548.
[52] E. Paparazzo, On the number, binding energies, and mutual intensities of Ce3d peaks in the XPS analysis of cerium oxide systems: A response to Murugan et al., Superlatt. Microstruct. 85 (2015) 321, Superlatt. Micro 105 (2017) 216–220.
[53] K.I. Maslakov, et al., **XPS study of ion irradiated and unirradiated CeO_2 bulk and thin film samples**, Appl. Surf. Sci. 448 (2018) 154–162.
[54] Y. Tezuka, et al., Electronic structure study of CaCu3Ti4O12 by means of X-ray Raman scattering, J. Electron. Spectrosc. Relat. Phenom. 220 (2017) 114–117.
[55] N. Kolev, et al., **Raman spectroscopy of $CaCu_3Ti_4O_{12}$**, Phys. Rev. B Condens. Matter 66 (2002) 1–4.
[56] R.C. Deus, et al., Electrical behavior of cerium dioxide films exposed to different gases atmospheres, Ceram. Int. 42 (2016) 15023–15029.
[57] I. Nurhasanah, AbdullahM., Khairurrijal. **Structure and Morphology of Neodymium-doped Cerium Oxide Solid Solution Prepared by a Combined Simple Polymer Heating and D.C.-Magnetron Sputtering Method**, AIP Conf. Proc. 989 (2008) 147–150.
[58] X. Li, et al., **Giant photostriction of $CaCu_3Ti_4O_{12}$ ceramics under visible light illumination**, Appl. Phys. Lett. 116 (2020) 4–9.
[59] R.V. Vendrinsckii, et al., Pre-edge fine structure of the 3d atom K X-ray absorption spectra and quantitative atomic structure determinations for ferroelectric perovskite structure crystals, J. Phys. Condens. Matter (10 () (1998) Article 9561.
[60] P.Y. Raval, et al., **A Ti L3,2 - and K- edge XANES and EXAFS study on Fe^{3+}-substituted $CaCu_3Ti_4O_{12}$**, Ceram. Int. 44 (2018) 20716–20722.
[61] F. Farges, G.E. Brown, J.J. Rehr, **Ti K -edge XANES studies of Ti coordination and disorder in oxide compounds: Comparison between theory and experiment**, Phys. Rev. B. 56 (1997) 1809–1819.
[62] V. Krayzman, et al., **Effects of local atomic order on the pre-edge structure in the Ti K x-ray absorption spectra of perovskite $CaTi_{1-x}Zr_xO_3$**, Phys. Rev. B. 74 (2006) 1–7.
[63] S. de Lazaro, et al., **Relation between photoluminescence emission and local order-disorder in the $CaTiO_3$ lattice modifier**, Appl. Phys. Lett. 90 (2007) 9–12.
[64] C. Ribeiro, et al., **Anisotropic growth of oxide nanocrystals: Insights into the rutile TiO_2 phase**, J. Phys. Chem. C. 111 (2007) 5871–5875.
[65] E. Swatsitang, T. Putjuso, **Improved non-ohmic and dielectric properties of Cr^{3+} doped $CaCu_3Ti_4O_{12}$ ceramics prepared by a polymer pyrolysis solution route**, J. Eur. Ceram. Soc. 38 (2018) 4994–5001.
[66] S.M. de Freitas, M.V. dos, S. Rezende, Effect of europium concentration on its distribution in the host sites of lithium tantalite, J. Phys. Chem. Solids 112 (2018) 158–162.
[67] S.M. de Freitas, et al., **Computational Condensed Matter Defects and dopant properties of $SrSnO_3$ compound: A computational study**, Comput. Condens. Matter 21 (2019) Article e00411.
[68] G.J. Barbosa Junior, et al., Investigation of Europium dopant in the orthophosphate KMPO4 (M = Ba and Sr) compounds, J. Phys. Chem. Solids 130 (2019) 282–289.
[69] W. Makcharoen, W. Punsawat, **Dielectric Relaxation and Microstructures of SnO_2 Doped $CaCu_3Ti_4O_{12}$ Electroceramics Prepared Via Vibro-milling Method**, Mater. Today.: Proc. 4 (2017) 6234–6238.
[70] M.V.D.S. Rezende, M.E.G. Valerio, R.A. Jackson, Modelling the concentration dependence of rare earth doping in inorganic materials for optical applications: Application to rare earth doped barium aluminate, Opt. Mater. 34 (2011) 109–118.
[71] H.R. Abd, et al., **Rapid synthesis of Ce^{3+}: YAG via CO_2 laser irradiation combustion method: Influence of Ce doping and thickness of phosphor ceramic on the performance of a white LED device**, J. Solid State Chem. (294) (2021) Article 121866.
[72] V. Khanin, et al., **Exciton interaction with Ce^{3+} and Ce^{4+} ions in $(LuGd)_3(Ga, Al)_5O_{12}$ ceramics**, J. Lumines 237 (2021) Article 118150.
[73] S.H. Yu, H. Cölfen, A. Fischer, **High quality CeO_2 nanocrystals stabilized by a double hydrophilic block copolymer**, Colloids Surf. A Physicochem. Eng. Asp 243 (2004), pp. 49–52.
[74] O.M. Ntwaeaborwa, P.H. Holloway, **Enhanced photoluminescence of Ce^{3+} induced by an energy transfer from ZnO nanoparticles encapsulated in SiO_2**, Nanotechnol 16 (2005) 865–868.
[75] L.F. da Silva, et al., **Relationship between crystal shape, photoluminescence, and local structure in $SrTiO_3$ synthesized by microwave-assisted hydrothermal method**, J. Nanomater. 2012 (2012) 25–28.

[76] S. Mochizuki, F. Fujishiro, **The photoluminescence properties and reversible photoinduced spectral change of CeO_2 bulk, film and nanocrystals**, Phys. Status Solidi (B) Basic Res 246 (2009) 2320–2328.
[77] F. Clabau, et al., **Mechanism of phosphorescence appropriate for the long-lasting phosphors Eu^{2+}-doped $SrAl_2O_4$ with codopants Dy^{3+} and B^{3+}**, Chem. Mater. 17 (2005) 3904–3912.
[78] K. Asami, et al., **Redshift and thermal quenching of Ce^{3+} emission in $(Gd, Y)_3(Al, Si)_5(O, N)_{12}$ oxynitride garnet phosphors**, Opt. Mater. 87 (2019) 117–121.
[79] M.V. Korzhik, et al., **Spectrocopy and origin of radiation centers and scintillation in $PbWO_4$** single cry**stals**, Phys. Stat. Sol. (A). 154 (1996) 779–788.